

A Modified 3D Biconical Outflow Model: Spatial Constraints on AGN-driven Outflows

CHANGSEOK KIM ¹ AND JONG-HAK WOO ^{1,2}

¹*Department of Physics and Astronomy, Seoul National University, 1 Gwanak-ro, Gwanak-gu, Seoul 08826, Republic of Korea*

²*SNU Astronomy Research Center, Seoul National University, 1 Gwanak-ro, Gwanak-gu, Seoul 08826, Republic of Korea*

ABSTRACT

We present a modified outflow model and its application to constrain ionized outflow properties of active galactic nuclei (AGNs). By adding a rotating disk component to the biconical outflow model of H.-J. Bae & J.-H. Woo (2016), we find that models with a rotating disk require faster launching velocities ($\lesssim 1500 \text{ km s}^{-1}$) than outflow-only models to be consistent with the observed gas kinematics of local type 2 AGNs. We perform Monte Carlo simulations to reproduce the observed distribution of gas kinematics of a large sample ($\sim 39,000$), constraining the launching velocity and opening angle. While the launching velocity is moderate for the majority of the local AGNs, the notable cases of 2 - 5 % show strong outflows with $V_{max} \sim 1000 - 1500 \text{ km s}^{-1}$. By examining the seeing effect based on the mock integral field unit data, we find that the outflow sizes measured based on velocity widths tend to be overestimated when the angular size of the outflow is comparable to or smaller than the seeing. This result highlights the need for more careful treatments of the seeing effect in the outflow size measurement, yet it still supports the lack of global feedback by gas outflows for local AGNs.

Keywords: Active galactic nuclei (16), Galaxy kinematics (602), Galaxy winds (626)

1. INTRODUCTION

Accreting supermassive black holes, or active galactic nuclei (AGNs), emit a vast amount of energy through various channels, i.e., radiation, gas outflows, and relativistic jets, which are thought to interact with the interstellar medium (ISM) and eventually affect star formation in host galaxies (e.g., J. Silk & M. J. Rees 1998; A. C. Fabian 2012). Recent theoretical studies commonly implement AGN feedback to reproduce primary observables, i.e., galaxy luminosity function (e.g., P. F. Hopkins et al. 2008; R. Weinberger et al. 2017; S. Wellons et al. 2023). Nonetheless, the overall role and detailed mechanism of AGN feedback remain unclear in observations (see reviews by C. M. Harrison 2017; C. M. Harrison & C. Ramos Almeida 2024).

AGN-driven gas outflows are widely considered as one of the primary candidates for a feedback channel. It is now well-known that these outflows are multiphase (e.g., F. Fiore et al. 2017; A. Fluetsch et al. 2019; R. A. Riffler et al. 2023), ubiquitous (e.g., J. R. Mullaney et al.

2013; J.-H. Woo et al. 2016; S. Rakshit & J.-H. Woo 2018), and kpc-scales (e.g., C. M. Harrison et al. 2014; C. Kim et al. 2023). In particular, the broad wing component of the [O III] $\lambda 5007$ emission line is frequently utilized to investigate kpc-scale warm ionized gas outflows (T. Boroson 2005; J. E. Greene & L. C. Ho 2005). Large spectral surveys such as Sloan Digital Sky Survey (SDSS) enabled the scrutiny of integrated outflow properties within the central region for several tens of thousands of AGNs and their correlations with host galaxy properties (e.g., J.-H. Woo et al. 2017, 2020).

On the other hand, using spatially resolved spectroscopy, many other studies have focused on the detailed outflow structures for a limited number of targets (\lesssim several tens). One of the primary findings in early studies is that the ionized outflows are well-described by a biconical model with two axisymmetric cones (D. M. Crenshaw & S. B. Kraemer 2000; D. M. Crenshaw et al. 2000; S. Veilleux et al. 2001; V. Das et al. 2005, 2006). Subsequent studies took into account the dust extinction by the galactic plane (e.g., D. M. Crenshaw et al. 2010a,b; T. C. Fischer et al. 2010, 2011, 2013; H.-J. Bae & J.-H. Woo 2016) or a rotating disk (e.g., F. Müller-Sánchez et al. 2011) to reproduce the [O III] line profile and diverse narrow line region (NLR) kinematics. C. Marconcini et al. (2023) recently developed a new mod-

Corresponding author: Jong-Hak Woo
woo@astro.snu.ac.kr

Email: kcs1996kcs@snu.ac.kr

eling tool for analyzing 3D gas kinematics based on the 3D distribution of numerous gas clouds. By using a sample of nearby AGNs, these studies have provided various constraints on the geometry, extent, and energetics of outflows, which are crucial for quantifying outflow energetics and their impact on the host galaxy evolution.

Despite the importance of estimating the outflow parameters, it is challenging to expand these works to a large sample due to observational limitations. For instance, spatially resolved spectroscopic observations are still too expensive to be applied to a large sample. Furthermore, while integral field unit (IFU) surveys such as MaNGA or SAMI provide spatially resolved kinematics for \lesssim thousands of AGNs (D. Wylezalek et al. 2020; A. Deconto-Machado et al. 2022; L. Gatto et al. 2024; S. Oh et al. 2024), they typically have a seeing-limited resolution (FWHM $\sim 1''$ - $2''$), which is often insufficient to resolve outflow structures at moderate redshifts. For example, a few kpc scales of outflows at $z \sim 0.1$ (1 kpc $\sim 0.5''$) are barely resolved even under the best seeing conditions on the ground. While space telescopes such as Hubble Space Telescope (HST) and James Webb Space Telescope (JWST) or adaptive optics (AO) can improve the spatial resolution down to a diffraction-limit (FWHM $\sim 0.1''$), the detailed geometry and kinematics can only be resolved in rare cases such as nearby AGNs (e.g., T. C. Fischer et al. 2013; G. E. Polack et al. 2024) or galactic scale outflows (e.g., A. Vayner et al. 2021; D. Wylezalek et al. 2022; G. Cresci et al. 2023).

Nevertheless, detailed outflow models and simulated mock data can be efficiently utilized to overcome the limited spatial resolution and constrain the physical parameters of the outflows, which are not directly measurable. H.-J. Bae & J.-H. Woo (2016) constructed a 3D biconical outflow model combined with a simple extinction by a thin dust plane and investigated the effect of each parameter on the gas kinematics. Their main findings are as follows: (1) velocity dispersion is higher for larger intrinsic outflow velocity or bicone inclination; (2) velocity offset with respect to systemic velocity increases with higher dust extinction; (3) a maximum velocity of 500 - 1000 km s $^{-1}$ can explain most of the observed gas kinematics of local SDSS type 2 AGNs from J.-H. Woo et al. (2016); and (4) higher intrinsic velocities tend to have wider bicone opening angles. However, this model did not account for rotating disk emission and seeing convolution, which are critical for reproducing 2D gas kinematics.

In this study, we present a 3D biconical outflow model modified from H.-J. Bae & J.-H. Woo (2016) along with applications of mock SDSS and IFU data. Comparing with observations, we provide spatial constraints on gen-

eral properties of gas outflows and discuss the effect of seeing and the rotating disk component. The paper is structured as follows. In Section 2, we summarize the original outflow model of H.-J. Bae & J.-H. Woo (2016) and describe three main modifications of this study. Section 3 describes procedures for generating mock SDSS and IFU data and their applications. In Section 4, we present the main results of the mock data analysis, including constraints on outflow properties. We discuss the implications of the main results and comparisons with other outflow models in Section 5. Lastly, we summarize the key conclusions in Section 6. In this paper, we adopt a standard Λ CDM cosmology with $H_0 = 67.8$ km/s/Mpc, $\Omega_\Lambda = 0.692$, and $\Omega_m = 0.308$.

2. MODIFIED 3D BICONICAL OUTFLOW MODEL

We summarize the original outflow model from H.-J. Bae & J.-H. Woo (2016) in Section 2.1 and demonstrate three major modifications in Section 2.2, 2.3, and 2.4, respectively.

2.1. 3D Biconical Outflow Model

H.-J. Bae & J.-H. Woo (2016) presented a 3D outflow model adopted from D. M. Crenshaw et al. (2010a,b), which consists of two axisymmetric outflow cones and a simple extinction factor by a thin galactic dust plane (see Figure 1). Once a set of 11 parameters is given, the model constructs 3D distributions of flux and velocity. By collapsing the 3D model along the line-of-sight (LOS), 2D distributions of flux, velocity, and velocity dispersion are generated. H.-J. Bae & J.-H. Woo (2016) also calculated flux-weighted velocity and velocity dispersion using the 2D maps for a direct comparison with the observed [O III] velocity and velocity dispersion (VVD) distribution of SDSS type 2 AGNs from J.-H. Woo et al. (2016).

The input parameters define the bicone structure, 3D distributions of flux and kinematics, and the orientations of the bicone and the dust plane. For the bicone structure, three parameters determine the outflow size (R_{out}) and inner and outer half opening angles (θ_{in} and θ_{out}). As illustrated by the dark gray region in Figure 1, we model gas outflows using a hollow bicone. For simplicity, we fix the difference between the outer and inner half opening angles to 20° ($\theta_{out} = \theta_{in} + 20^\circ$). While the opening angle differences estimated by T. C. Fischer et al. (2013) are mostly in the 5° - 20° range, they adopted the minimum opening angle difference required to match the observations, meaning that the larger difference is also plausible. Thus, we adopted 20° as a representative value from observations. We also note that the inner opening angle has an opposite, but less sig-

nificant effect on the integrated kinematics compared to the outer opening angle (H.-J. Bae & J.-H. Woo 2016).

The flux distribution is determined by e -folding radius (τ), i.e., a radius where the flux decreases by a factor of e , and dust extinction factor (A). Since we only focus on relative flux distributions, we adopt an arbitrary central flux value (f_0). We assume that the intrinsic 3D flux distribution follows an exponential form based on the distance from the center (R). Thus, the intrinsic 3D flux distribution can be written as $f(R) = f_0 e^{-R/\tau}$. Following H.-J. Bae & J.-H. Woo (2016), we assume the e -folding radius is 20% of the outflow size ($\tau = R_{out}/5$), which gives approximately two orders of magnitude fainter flux at the outflow edge than at the center. The dust extinction factor is multiplied when collapsing the 3D flux distributions to 2D flux maps. If a voxel is located behind the galactic dust plane along the LOS, its flux will be dimmed by the extinction factor in the 2D map. The opening angles and the relative inclination compared to the galactic plane decide which voxels are subject to dust extinction.

The 3D velocity distributions are determined by two parameters, i.e., maximum velocity (V_{max}) and velocity profile. There are three options for the velocity profile as a function of the distance from the center (R): (1) a linear increase case ($v(R) = V_{max}(R/R_{out})$); (2) a linear decrease case ($v(R) = V_{max}(1 - R/R_{out})$); and (3) a constant velocity ($v(R) = V_{max}$). In all three cases, the velocity is directed radially outward from the center. Following H.-J. Bae & J.-H. Woo (2016), we adopt the linear decrease case for all models in this study. Note that the maximum velocity can be regarded as a launching velocity, as it represents the intrinsic outflow velocity at the center. This 3D velocity distribution is then collapsed to the 2D velocity and velocity dispersion maps in a flux-weighted manner as follows:

$$V(x, y) = \frac{\int v_p(x, y, z) f(x, y, z) dz}{\int f(x, y, z) dz}, \quad (1)$$

$$\sigma^2(x, y) = \frac{\int v_p^2(x, y, z) f(x, y, z) dz}{\int f(x, y, z) dz} - V^2(x, y) \quad (2)$$

where $V(x, y)$ and $\sigma(x, y)$ are 2D distributions of velocity and velocity dispersion in the (x, y) sky plane (see example 2D maps in the top row of Figure 2). $f(x, y, z)$ and $v_p(x, y, z)$ are 3D flux and projected velocity values at (x, y, z) voxel. The LOS is defined as the z -axis in this coordinate system.

Lastly, the orientations of the model are determined by position angles (PAs; PA_{cone} and PA_{disk}) and inclinations (i_{cone} and i_{disk}) of the bicone and the dust plane

(or disk in Section 2.2). The orientations of the bicone and the dust plane are independent of each other, allowing them to rotate freely on the sky plane. However, for simplicity, we fix the PAs of the bicone and dust plane to 0° and 90° , respectively, meaning that the bicone axis and the major axis of the plane extend along the north-south and east-west directions, respectively. Since our mock data analysis focuses on $3''$ -extracted kinematics and radial profiles of velocity widths, the effect of PAs is negligible.

Note that we do not consider various relative PA values between the disk and bicone for simplicity. We expect that the relative PA has no significant effect on mock SDSS data since we integrate all pixels within the $3''$ -aperture. In addition, velocity widths in mock IFU analysis are dominated by the bicone component in cases of strong outflows, thereby reducing the impact of the rotational orientation of the disk on the kinematics. The effect of relative PAs on mock IFU data will be investigated in future work.

Using this biconical model, H.-J. Bae & J.-H. Woo (2016) tested the impact of each parameter on the velocity offset and dispersion, and the line profile of the [O III] emission line. Nevertheless, the model lacked several components crucial for comparison with observational data. For instance, it did not consider rotating gas in a galactic disk, which is thought to mainly contribute to the narrow/core component of the typical [O III] line profile. Furthermore, to accurately compare the spatial properties of the simulated outflows with observations, the seeing convolution should be taken into account. Therefore, we add a rotating gas component (Section 2.2) and the seeing effect (Section 2.3) to the H.-J. Bae & J.-H. Woo (2016) model. In addition, to improve mock data compatibility, we switch from a coordinate system normalized by the outflow size to a physical scale in arcsec units based on the redshift and outflow size parameters (Section 2.4).

2.2. Rotating Component

While outflows are the dominant nongravitational component in AGN kinematics, the gas motions in the NLR are more complex due to additional dynamical effects. In particular, gas motion due to the gravitational potential of the host galaxy is represented by a core component of narrow emission lines, which show similar line width and offset compared to stellar absorption lines ($\sigma_{[\text{OIII}], narrow} \sim \sigma_*$; C. H. Nelson & M. Whittle 1996; J. E. Greene & L. C. Ho 2005). If there is no nongravitational effect, gas kinematics are governed by a host galaxy potential, i.e., a rotating disk (e.g., R. Luo et al. 2019). Given that a majority of AGNs in the VVD

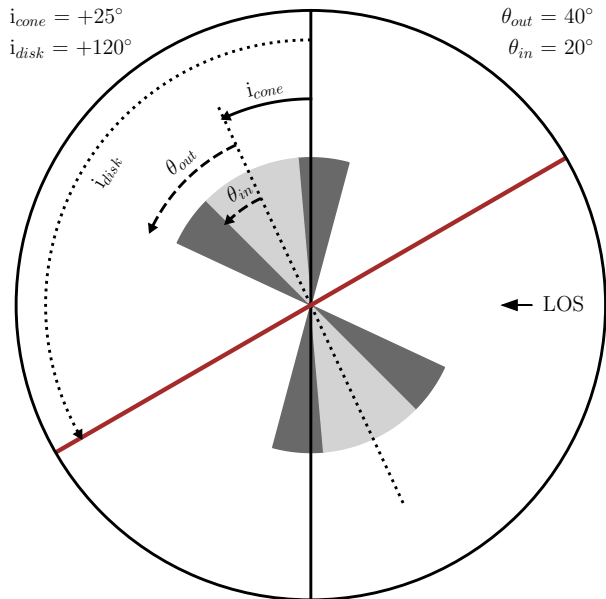


Figure 1. Example biconical outflow model from H.-J. Bae & J.-H. Woo (2016). The dust plane is shown as a red line between the two cones. The dark gray region represents the volume occupied by the outflowing gas (i.e., between inner and outer opening angles), while the light gray region denotes the hollow interior. The LOS direction is indicated by the black arrow. The definitions and adopted values of the cone and disk inclination angles are also shown.

diagram (see Figure 4(a)) show relatively small velocity offset and dispersion, the disk component should be included to reproduce the observed distribution of the gas kinematics properly. Even for AGNs with strong outflows, a rotational pattern is often observed in IFU data (D. Kang & J.-H. Woo 2018; C. Kim et al. 2023). Thus, a disk component is required to reproduce the characteristics in the spatially resolved kinematics.

To generate disk models, we use the `GalPak`^{3D} package (Galaxy Parameters and Kinematics, N. Bouché et al. 2015), which was originally developed for the morphokinematics of 3D observational data. Since our goal is to investigate the effect of a rotating disk on the observed gas kinematics, we employ only the basic models generated by the package without adjusting details. Using the default models of `GalPak`^{3D}, we assume radial and perpendicular flux profiles as exponential ($n = 1$) and Gaussian, respectively, and set the rotation curve to a hyperbolic tan (\tanh) profile.

We regulate two flux parameters (f_{disk}/f_{cone} and $r_{1/2}$) and three kinematic parameters ($V_{max,rot}$, r_t , and σ_0) of the disk model. The inclination and PA of the disk are assumed to be the same as those of the dust plane in the outflow model. For the flux, the total disk flux within the SDSS fiber size ($3''$) is first determined by the

disk-to-cone flux ratio parameter (f_{disk}/f_{cone}) and the integrated flux of the outflow. We then determine the disk flux distribution by assuming an exponential disk with a given half-light radius parameter ($r_{1/2}$).

For the gas kinematics, the maximum rotational velocity ($V_{max,rot}$) and the turnover radius (r_t) determine the velocity profile with a \tanh function as follows:

$$v(r) = V_{max,rot} \tanh(r/r_t), \quad (3)$$

where r is the radius on the galactic plane. At $r > r_t$, the rotational velocity begins to follow a flat radial profile. In addition, we adjust the intrinsic velocity dispersion (σ_0), which corresponds to the dynamical hotness of the disk.

Once the five disk parameters and the disk orientation (PA_{disk} and i_{disk}) are given, `GalPak`^{3D} computes flux, velocity, and velocity dispersion maps. We then sum the 2D flux maps of the outflow and disk models. For velocity and velocity dispersion maps, we combine them by flux-weighted means. In Figure 2, the second row shows mock 2D maps of the disk model for an example with $i_{disk} \sim 120^\circ$ at $z = 0.05$. We assume a stellar mass of $\sim 10^{10.5} M_\odot$, which corresponds to the following parameters: $V_{max,rot} = 198 \text{ km s}^{-1}$, $r_{1/2} = 5.2 \text{ kpc}$, $\sigma_0 \sim 117 \text{ km s}^{-1}$, $r_t \sim 2.5 \text{ kpc}$. The third row of Figure 2 shows the combined maps of the outflow and disk models with $f_{disk}/f_{cone} = 1$. These combined maps demonstrate that the biconical structure is properly embedded in the background disk model.

2.3. Seeing Effect

The beam smearing effect by atmospheric seeing has been pointed out as a significant obstacle in spatially resolved studies of AGNs (e.g., B. Husemann et al. 2016; M. Villar-Martín et al. 2016; M. Singha et al. 2022). Given that the seeing effect is more pronounced at higher redshifts, we need to include it in our model to account for outflows in a majority of AGN host galaxies.

To reproduce more realistic 2D maps, we convolve the combined 2D maps with a Gaussian kernel as follows:

$$G(x, y) = \frac{1}{2\pi\sigma_g^2} \exp\left(-\frac{x^2 + y^2}{2\sigma_g^2}\right) \quad (4)$$

where σ_g is a seeing size parameter ($\sigma_g = \text{FWHM}/(2\sqrt{2\ln 2})$). In this study, we adopt two cases of the seeing size, $0.8''$ and $1.5''$. The former is a typical seeing size of high resolution optical IFU data, while the latter is a median seeing size in SDSS. The convolved 2D maps are calculated as follows:

$$F_c(x, y) = F(x, y) * G(x, y), \quad (5)$$

$$V_c(x, y) = \frac{(V(x, y) \times F(x, y)) * G(x, y)}{F_c(x, y)}, \quad (6)$$

$$\begin{aligned} & \sigma_c^2(x, y) \\ &= \frac{((V^2(x, y) + \sigma^2(x, y)) \times F(x, y)) * G(x, y)}{F_c(x, y)} \\ & - V_c^2(x, y) \end{aligned} \quad (7)$$

where $F_c(x, y)$, $V_c(x, y)$, and $\sigma_c(x, y)$ are convolved flux, velocity, and velocity dispersion, respectively. In the bottom row of Figure 2, we show an example of convolved 2D maps. The red horizontal bar on the upper right represents the applied seeing size in this example (FWHM = 0.8"). The seeing convolution blurs the central bicone structure, so the final images are more like a circular shape in all 2D maps. We will discuss the seeing effect in Section 4.3 and 5.3, focusing on implications for the outflow size measurements in IFU data.

2.4. Mock Data Compatibility

We update our model to calculate 2D maps in an (x, y) coordinate system defined in arcsec units based on the input redshift and physical size of the outflow, while the H.-J. Bae & J.-H. Woo (2016) model adopted relative scales normalized by the outflow size. This approach offers several advantages: (1) the outflow model uses the same pixel units as the disk model, making it convenient to combine the two models; (2) mock data can be directly compared with real observational data. Accordingly, we specify the mock data by pixel size and field-of-view (FoV) parameters, and all calculations are performed using this pixel scale from given redshift and physical length parameters (R_{out} , $r_{1/2}$, and r_t).

3. MOCK DATA ANALYSIS

In this Section, we describe our main analysis procedures based on mock data generated from the modified outflow model. First, we generate mock SDSS data extracted from the central 3"-aperture, and compare them with the observed [O III] kinematics of a large sample of SDSS type 2 AGNs in Section 3.1. In Section 3.2, we produce mock IFU data to analyze outflow sizes and 2D distributions of flux, velocity, and velocity dispersion.

3.1. Mock SDSS Data

H.-J. Bae & J.-H. Woo (2016) integrated the [O III] velocity offset and dispersion within the outflow radius and compared them with the observed VVD distribution of ~39,000 SDSS type 2 AGNs from J.-H. Woo et al. (2016). Here, we use our modified model to reexamine the comparison with the observed VVD distribution.

To simulate SDSS spectra, we calculate the integrated velocity offset and dispersion (v_{int} , σ_{int}) within the central 3"-aperture shown as gray circles in Figure 2. In this example ($z = 0.05$ and $R_{out}=3$ kpc), the projected size of the bicone exceeds the SDSS fiber region, so its outer part is not included in the mock SDSS data. While this rarely occurs for models with low redshifts and large outflow sizes, it provides a representative example of how modifications affect the mock data.

As we integrate the kinematics within an aperture twice as large as the FWHM of the seeing (1.5"), the seeing convolution does not significantly impact the VVD distributions. On the other hand, the rotating gas component influences the integrated velocity offset and dispersion since it has a velocity offset near zero and a narrow width with comparable flux to the outflow component. Thus, we mainly investigate the effect of the rotating gas component on the VVD distribution.

3.1.1. Model Grids for the Observed VVD

To investigate the effect of outflow properties on the observed kinematics, we overlay various model grids on the observed VVD diagram. We mainly investigate five parameters: the dust extinction factor (A), opening angles (θ_{out} and θ_{in}), bicone inclination (i_{cone}), launching velocity (V_{max}), and disk-to-cone flux ratio (f_{disk}/f_{cone}). We fix the disk inclination as 60°, the outflow size as 1 kpc, and the stellar mass as $10^{10.5} M_{\odot}$.

We first compare the models with and without the rotating disk component. Then we adjust the bicone inclination while keeping the opening angle fixed, and vice versa. We change the bicone inclination from -40° to 0° and the outer half opening angle from 30° to 60° with a 10° step. For each model grid, we also adjust the dust extinction rate from 0 to 100 % (i.e., $A = 1$ to 0) and launching velocities by 500, 1000, and 2000 km s⁻¹.

3.1.2. Mock VVD from Monte Carlo Simulation

We perform Monte Carlo (MC) simulations and generate mock VVD distributions by assuming a probability distribution function (PDF) of each parameter. The primary purpose of these MC simulations is to identify the best PDFs of the launching velocity and opening angle parameters that reproduce the observed VVD distribution, and ultimately, to constrain these outflow properties for the type 2 AGN sample.

We first take PDFs of various parameters, such as redshift, stellar mass, disk-to-cone flux ratio, and extinction, from the observed SDSS type 2 AGNs (see Figure 3). The PDF of redshift (0.04 to 0.28 with 0.04 steps) is directly applied to the MC simulations. The observed disk-to-cone flux ratio is determined by the flux ratio between broad/wing and narrow/core components

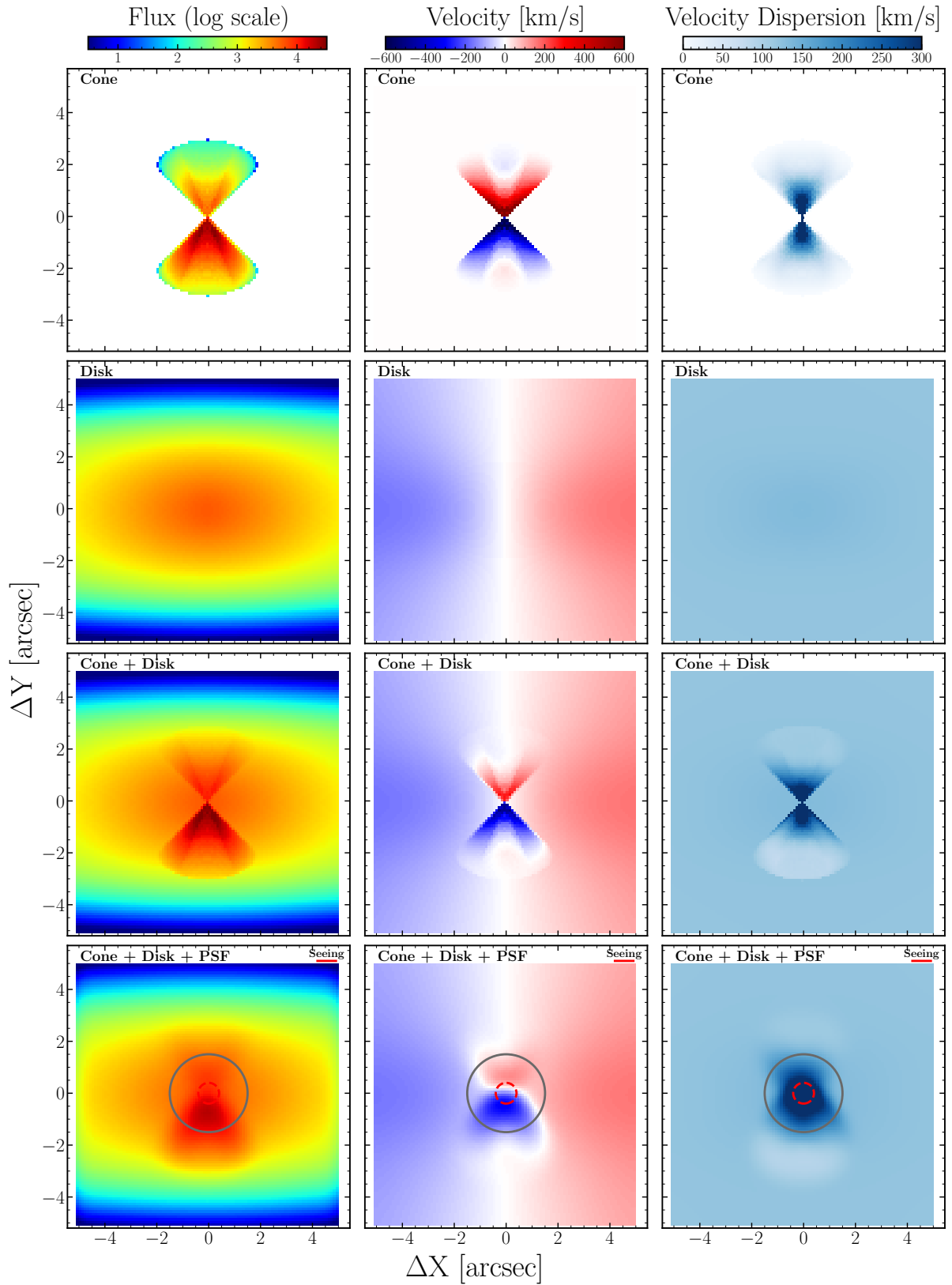


Figure 2. Examples of 2D maps produced by the modified model. From left to right, each column shows the flux, velocity, and velocity dispersion maps. The first row presents the biconical outflow model of H.-J. Bae & J.-H. Woo (2016). The second row shows the rotating disk model generated with GalPak^{3D}. The third row displays the combined bicone + disk model, and the last row presents the combined model after applying the seeing convolution. Red dashed circles at the center, and red bars in the upper-right corner indicate the FWHM of the seeing. Gray circles denote the 3'' aperture corresponding to the SDSS fiber size.

when the [O III] line is fitted with a double Gaussian. If the [O III] line is fitted with a single Gaussian, we classify the emission as either disk-only or outflow-only based on the difference between stellar and [O III] velocity dispersion. Specifically, when $|\sigma_{[\text{O III}]} - \sigma_*|$ is less than 30 km s^{-1} , we classify this single Gaussian as disk-only emission, i.e., $f_{\text{disk}}/f_{\text{cone}} = \infty$, otherwise as outflow-only emission, i.e., $f_{\text{disk}}/f_{\text{cone}} = 0$. We also estimate the PDF of the dust extinction factor by using observed $H\alpha/H\beta$ with $R_V^A = 4.5$ (F. P. A. Vogt et al. 2013). Note that we restrict the dust extinction rate to smaller than 80% (or $A > 0.2$) since a higher extinction rate results in too broad mock VVD distributions along the $V_{[\text{O III}]}$ axis, which are inconsistent with the observed distribution. Furthermore, an extinction rate higher than 80% is an extreme case, corresponding to $A_{\lambda 5007} \gtrsim 1.75 \text{ mag}$.

The stellar mass is taken from the MPA-JHU catalog³ and divided into five bins ($\log M_* = 9.7$ to 11.3 with 0.4 step). We calculate the four remaining disk parameters, i.e., $r_{1/2}$ (A. A. Dutton et al. 2011), $V_{\text{max,rot}}$ (S. Torres-Flores et al. 2011), σ_0 (S. Oh et al. 2022), and r_t (N. C. Amorisco & G. Bertin 2010), using empirical relations with stellar mass. Thus, once the stellar mass is selected among the five values, these four disk parameters are determined accordingly. Note that we restrict our sample to type 2 AGNs in the MC simulations due to the large uncertainties in stellar mass for type 1 AGNs.

For the outflow model, we first adopt random inclinations and fixed PAs ($\text{PA}_{\text{cone}}=0^\circ$ and $\text{PA}_{\text{disk}}=90^\circ$) for both the bicone and dust plane. The inclination of the dust plane is given from 7.5° to 172.5° with a 15° step, and its PDF is proportional to the solid angle of the normal vector integrated from 0° to 360° of PA. Since we focus on type 2 AGNs, we restrict the bicone inclination to less than 40° (7.5° , 22.5° , and 37.5°), and its PDF is also proportional to the solid angle of the bicone axis. Models with higher bicone inclinations, i.e., more aligned bicone axis with the LOS, are likely to be observed as type 1 AGNs, as their accretion disk and broad line region (BLR) are readily exposed to the observer (e.g., F. Marin 2014). Then we assume that the PDF for five outflow size values (0.3, 1, 3, 6, 9 kpc) follows a Gaussian distribution with a mean of zero and a standard deviation of 2 kpc. Note that the outflow size has little effect on the kinematics in mock SDSS data.

Our main goal is to constrain two parameters, i.e., the launching velocity and opening angle of the outflow model. For these two parameters, we assume that their PDFs follow a truncated Gaussian function. We first

set the range of the launching velocity to $[100, \infty) \text{ km s}^{-1}$ and restrict the outer opening angle values from 30° to 70° with a 10° step based on T. C. Fischer et al. (2013). Note that larger outer opening angles are excluded due to their physically extreme geometry, while smaller opening angles are excluded since they do not improve the main results. We then run multiple MC simulations by changing the mean and standard deviation of the Gaussian to find the best V_{max} and θ_{out} distributions that generate the best-matching mock VVD with the observed VVD. Each MC simulation generates 100,000 pairs of velocity offset and dispersion.

3.1.3. Kullback-Leibler Divergence and D_{max}

To quantitatively compare the mock VVDs with the observed VVD, we apply two statistical quantities that assess proximity between two 2D distributions. We first calculate Kullback-Leibler (KL) divergence ($D_{KL}(P||Q)$, S. Kullback & R. A. Leibler 1951) as follows:

$$D_{KL}(P||Q) = \sum P(v_{\text{obs}}, \sigma_{\text{obs}}) \log \frac{P(v_{\text{obs}}, \sigma_{\text{obs}})}{Q(v_{\text{int}}, \sigma_{\text{int}})}, \quad (8)$$

where $P(v_{\text{obs}}, \sigma_{\text{obs}})$ and $Q(v_{\text{int}}, \sigma_{\text{int}})$ are probability distributions of the observed and mock VVD, respectively. In brief, the KL divergence is a measure of a statistical distance between two PDFs derived from information theory, i.e., the smaller the KL divergence is, the more similar the two PDFs are.

The second quantity is the D_{max} from the 2D Kolmogorov-Smirnov test, calculated from the public code NDTEST⁴. Like the 1D Kolmogorov-Smirnov test, it calculates the maximum absolute difference between two cumulative distribution functions (D_{max}) and performs a p-value test of whether two PDFs originate from the same distribution. Although all p-values are too small to conclude that the observed and mock VVDs are identical distributions, we utilize the D_{max} value to compare the relative superiority between the mock VVDs.

Note that we add random error smoothing to all mock VVDs based on typical SDSS uncertainties of velocity offset and dispersion to account for the observational uncertainties. To remove variations induced by this error smoothing, we repeat this process 100 times in each grid of V_{max} and θ_{out} PDFs and take the mean and standard deviation of KL divergence and D_{max} values. If the mean KL divergence (or D_{max}) for given parameter distributions is notably smaller than for the others, by more than its standard deviation, then that mock

³ <https://wwwmpa.mpa-garching.mpg.de/SDSS/>

⁴ Written by Zhaozhou Li, <https://github.com/syrte/ndtest>

VVD distribution is considered a better reproduction of the observed data.

3.2. Mock IFU Data

We simulate mock 2D maps using various redshifts and outflow sizes to test the validity of previous methods for outflow size measurements. In particular, we focus on the dependence of the measured sizes on the seeing size normalized by the angular size of the outflow.

In our previous IFU studies, we developed a kinematic approach to measure the outflow size and applied it to AGNs at $z < 0.3$ (M. Karouzos et al. 2016; D. Kang & J.-H. Woo 2018; H.-J. Bae et al. 2017; R. Luo et al. 2021; C. Kim et al. 2023). The outflow region is defined as where the [O III] velocity dispersion is more enhanced than stellar velocity dispersion, which traces the gravitational potential of the host galaxies. Specifically, we first plot a radial profile of ratios between the [O III] and stellar velocity dispersion ($\sigma_{[\text{O III}]} / \sigma_*$) and define the outflow size as a radius where the ratio becomes unity. Then we quadratically subtract the seeing size (σ_g) from the outflow size to correct the seeing effect.

We apply the same procedure to mock IFU data and compare the measured outflow size with the input outflow size. Since we do not have stellar velocity dispersion in our model, we alternatively adopt the [O III] velocity dispersion extracted within a $3''$ -aperture of the convolved disk-only maps. This velocity dispersion of the disk model mimics the [O III] narrow/core component, which is an optimal proxy of stellar velocity dispersion (e.g., J. E. Greene & L. C. Ho 2005).

Another widely used method for outflow size measurements is W_{80} -based method (e.g., C. M. Harrison et al. 2014; D. Wylezalek et al. 2020; D. Ruschel-Dutra et al. 2021), where W_{80} is defined as a [O III] line width including 80% of the total line flux. Similar to the $\sigma_{[\text{O III}]}$ -based method, the W_{80} -based method defines the outflow region where the W_{80} is broader than a certain criterion, frequently set to 600 km s^{-1} . Thus, the outflow size is determined as the radius of the furthest pixel from the center with W_{80} larger than 600 km s^{-1} .

To perform the W_{80} -based analysis to mock IFU data, we create mock 3D cube data by adding a spectral axis. We assume that the bicone and disk components are observed as individual Gaussians that have the same flux, velocity, and velocity dispersion at each position in the convolved 2D maps. As a result, we obtain the double Gaussian line profile of each pixel, consisting of a narrow/core component from the convolved disk map and a broad/wing component from the convolved bicone map. Then we calculate W_{80} values of all pixels and

determine the outflow size as the radius of the furthest pixel from the center with $W_{80} > 600 \text{ km s}^{-1}$.

4. RESULT

4.1. Location of Model Grids in VVD Diagram

We investigate the dependency of outflow parameters on the location in the VVD diagram by comparing model grids with observations. The observed VVD distribution of local type 2 AGNs (Figure 4(a)) is characterized by a V-shaped envelope and a larger number of blueshifted than redshifted [O III] sources (J.-H. Woo et al. 2016).

First, we examine the influence of the rotating disk component by comparing model grids with and without disk emission (Figure 4(b)). Including the disk component reduces both the integrated velocity offset and dispersion (v_{int} and σ_{int}), because the disk typically exhibits smaller velocity offsets and dispersions than the outflow. As a result, the combined model requires a higher launching velocity up to 1500 km s^{-1} to reproduce the observed VVD distribution, whereas the original outflow-only model (H.-J. Bae & J.-H. Woo 2016) could explain most AGNs with V_{max} up to 1000 km s^{-1} (orange dashed lines).

Second, we revisit the effects of bicone inclination and dust extinction (Figure 4(c)). Both v_{int} and σ_{int} increase with larger inclination angles, consistent with H.-J. Bae & J.-H. Woo (2016). Increasing extinction decreases σ_{int} but increases v_{int} , owing to the reduced contribution from the receding cone. Notably, the $|v_{\text{int}}|/\sigma_{\text{int}}$ ratio is generally smaller than in the outflow-only model because the disk component has zero intrinsic velocity offset.

Lastly, we investigate the effect of the opening angle (Figure 4(d)). A wider opening angle produces a larger σ_{int} due to the broader distribution of LOS velocities, while v_{int} remains nearly constant. Overall, the dependence on opening angle is consistent with the trends reported by H.-J. Bae & J.-H. Woo (2016).

4.2. Constraints on V_{max} and θ_{out} Distributions

We constrain the distributions of V_{max} and θ_{out} by comparing the simulated VVD distributions with the observed VVD distribution. We perform multiple MC realizations, adopting Gaussian PDFs in which the mean and standard deviation of V_{max} range from 150 to 450 km s^{-1} and from 250 to 450 km s^{-1} , respectively, in steps of 50 km s^{-1} . For θ_{out} , we use mean values of 30° , 40° , and 50° , and standard deviations of 5° , 10° , and 20° . We note that the adopted means and standard deviations do not correspond exactly to those of the resulting PDFs because the distributions are truncated Gaussians. We then calculate 4D arrays containing 315 values ($7 \times 5 \times 3 \times 3$) for the KL divergence and D_{max} ,

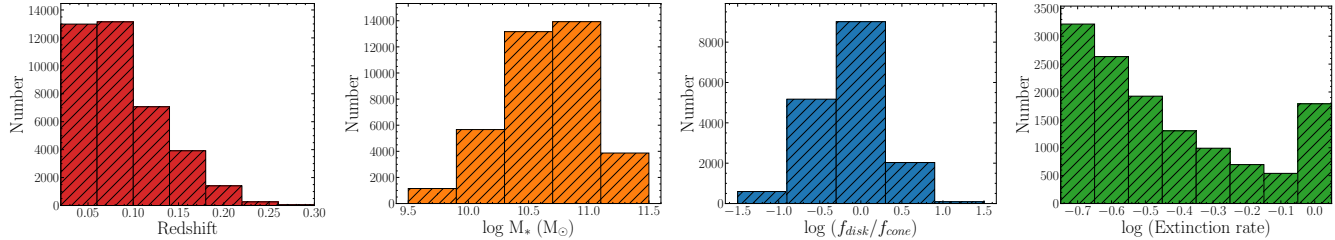


Figure 3. Histograms of physical properties of the type 2 AGN sample from J.-H. Woo et al. (2016). From left to right, the panels show the distributions of redshift, stellar mass, flux ratio between disk and outflow components, and extinction factor derived from the Balmer decrement.

and identify the best PDFs where these values are minimized. As a result, KL divergence is minimized when the launching velocity follows $(\mu_V, \sigma_V) = (250 \text{ km s}^{-1}, 400 \text{ km s}^{-1})$ and the opening angle follows $(\mu_\theta, \sigma_\theta) = (30^\circ, 10^\circ)$. D_{max} exhibits a minimum value when the launching velocity follows $(\mu_V, \sigma_V) = (350 \text{ km s}^{-1}, 300 \text{ km s}^{-1})$ and the opening angle follows $(\mu_\theta, \sigma_\theta) = (30^\circ, 5^\circ)$.

We first investigate variations in the KL divergence and D_{max} values depending on the input launching velocity and outer opening angle PDFs in Figures 5 and 6. For visualization, we collapse the 4D arrays into 2D maps by fixing the other parameter to its best PDF. The KL divergence and D_{max} maps of the launching velocity show local minima near the center, ruling out the lower left and upper right corners. This indicates that the observed VVD distribution generally prefers a moderate range of launching velocity. On the other hand, the opening angle PDF favors small values (i.e., lower left corner regions in Figure 6).

We present the best mock VVD distributions based on KL divergence (left) and D_{max} (right) in Figure 7. The two best mock VVD distributions are generally consistent with the observed one, reproducing both the V-shape feature and the overall range of the $V_{[\text{OIII}]}$ and $\sigma_{[\text{OIII}]}$. The best mock VVD distribution based on KL divergence exhibits a slightly larger $\sigma_{[\text{OIII}]}$ range than D_{max} . Despite the extinction limit ($A \geq 0.2$), the V-shape envelope of the mock VVD distribution is slightly broader than the observed one, especially in the low $\sigma_{[\text{OIII}]}$ regime. This may result from several factors, such as large observational uncertainties for weak outflow AGNs.

The histograms in Figure 8 show the best PDFs of the launching velocity based on the KL divergence (left) and D_{max} (right). The two quantities adopt similar best PDFs for the launching velocity. As predicted in Section 4.1, the launching velocities are mostly smaller than 1000 km s^{-1} , while 2 - 5% exhibit higher launching velocities ($1000 - 1500 \text{ km s}^{-1}$).

In contrast, strong outflow AGNs exhibit significantly different V_{max} distribution from the total sample. The

histograms in Figure 9 represent V_{max} distributions of strong outflow AGNs, which are located outside the dashed boxes in Figure 7 ($|V_{[\text{OIII}]}| > 300 \text{ km s}^{-1}$ or $\sigma_{[\text{OIII}]} > 400 \text{ km s}^{-1}$). Compared to the total distributions, strong outflow cases have fast launching velocities, mostly $800 - 1500 \text{ km s}^{-1}$. Since these AGNs are primary targets in spatially resolved studies, this result constrains a typical range of their launching velocities.

Lastly, the best PDFs of the opening angle (Figure 10) are slightly different depending on the statistical quantities. Specifically, $\theta_{out} \geq 50^\circ$ is only exhibited in the best PDF based on the KL divergence, while the best PDF based on D_{max} is concentrated on $\theta_{out} = 30^\circ - 40^\circ$. Nevertheless, the two best PDFs consistently favor relatively narrow outer opening angles, indicating that the opening angle of the local type 2 AGN is likely to be narrow, mostly $30^\circ - 40^\circ$.

4.3. Testing Outflow Sizes

We investigate the validity of the outflow size measurements based on mock IFU data by testing the effect of seeing. We set two examples of the same physical properties except for their redshifts (0.05 vs 0.3, see Table 1) to contrast the angular sizes of the outflows by a factor of \sim five for a given seeing (FWHM = $0.8''$).

We present the spatial distributions of velocity widths of the two examples in Figure 11 and 12. In our previous IFU studies, radial profiles of velocity dispersion often exhibit constant values in the central region (i.e., initial plateau) before a smooth decrease (e.g., M. Karouzos et al. 2016; D. Kang & J.-H. Woo 2018). This initial plateau is well reproduced in our mock IFU data, for both $\sigma_{[\text{OIII}]}$ (yellow) and W_{80} (blue). Moreover, the radius of the initial plateau is comparable to the HWHM of the seeing (red dashed line), indicating that it mainly results from the seeing effect.

In the low redshift case (Figure 11), since the angular outflow size is larger than the seeing by more than a factor of two, the measured outflow size is consistent with the input value, indicating that the outflow size is well recovered by applying the velocity-width-based methods. In contrast, in the high redshift case (Figure 12),

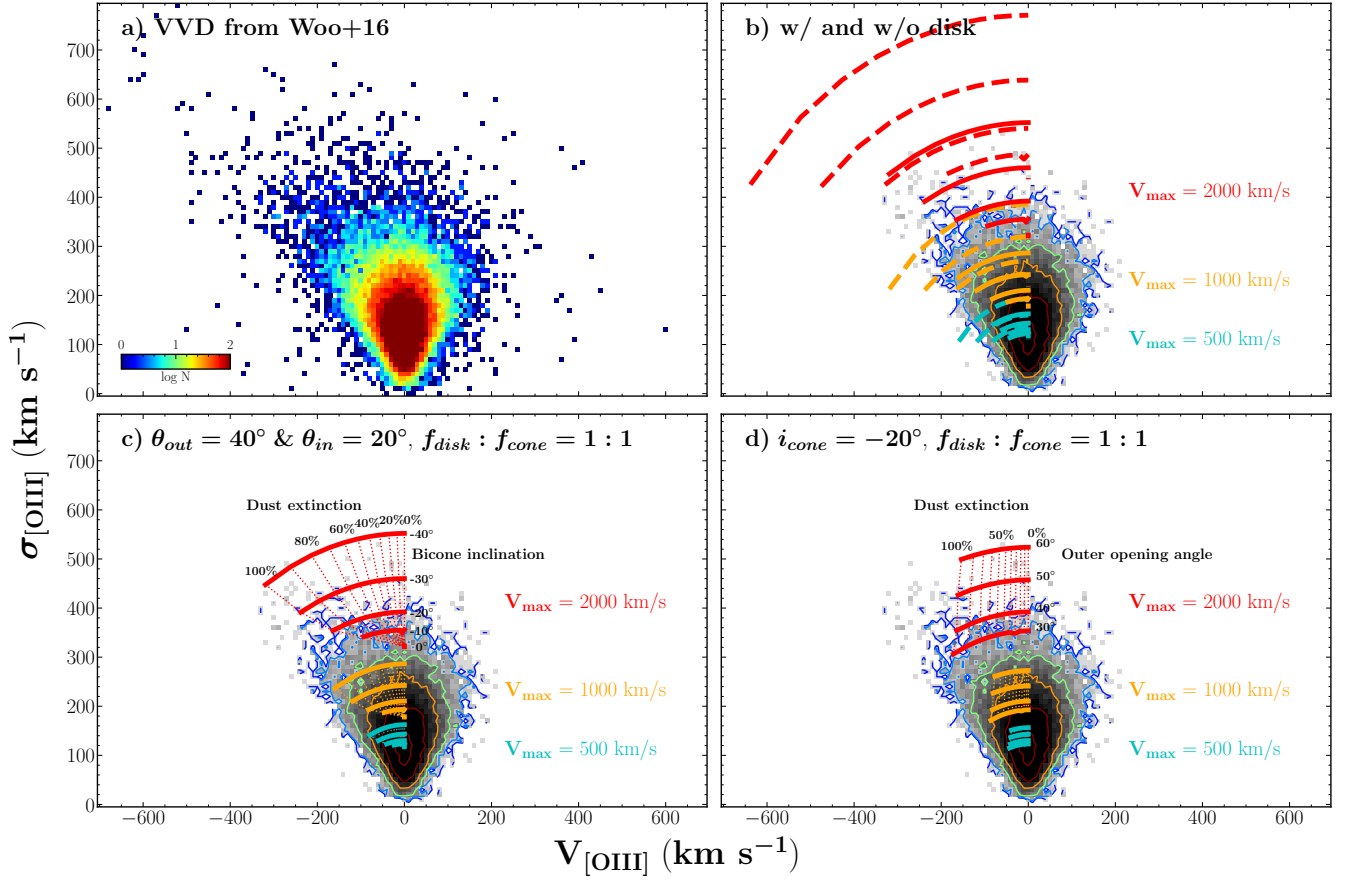


Figure 4. Model grids with a fixed launching velocity of 500 km s^{-1} (cyan), 1000 km s^{-1} (yellow), and 2000 km s^{-1} (red). (a) Observed [O III] VVD distribution of 39,000 type 2 AGNs from J.-H. Woo et al. (2016); the color scale indicates the number of AGNs in each bin. This distribution is also shown as contours and gray heat maps in panels (b)–(d). (b) Model grids with (solid lines) and without (dashed lines) the disk component. Each line traces the change in kinematics as a function of the extinction at a fixed inclination. (c) Model grids showing the effects of bicone inclination and extinction when the disk component is included. Solid lines indicate variations with extinction at a fixed inclination, while dotted lines indicate variations with inclination at a fixed extinction. (d) Model grids with different opening angles and extinction values. For clarity, solid and dotted lines denote models with fixed opening angles and fixed extinction values, respectively.

Table 1. Model Parameters for Mock IFU Analysis

z	R_{out}	V_{max}	θ_{out}	i_{cone}	i_{disk}	A	f_{disk}/f_{cone}	r_t	σ_0	$V_{max,rot}$	$r_{1/2}$
[1]	[2]	[3]	[4]	[5]	[6]	[7]	[8]	[9]	[10]	[11]	[12]
0.05 vs 0.3	1 kpc	1250 km s^{-1}	40°	25°	120°	0.2	1	2.5 kpc	117 km s^{-1}	198 km s^{-1}	5.2 kpc

NOTE—(1) Redshift; (2) outflow size; (3) maximum (launching) velocity; (4) outer opening angle; (5) bicone inclination; (6) disk (and dust plane) inclination; (7) extinction factor (smaller value means more extinction); (8) flux ratio between disk and bicone components; (9) velocity turnover radius (disk); (10) intrinsic velocity dispersion (disk); (11) maximum rotational velocity (disk); (12) effective radius.

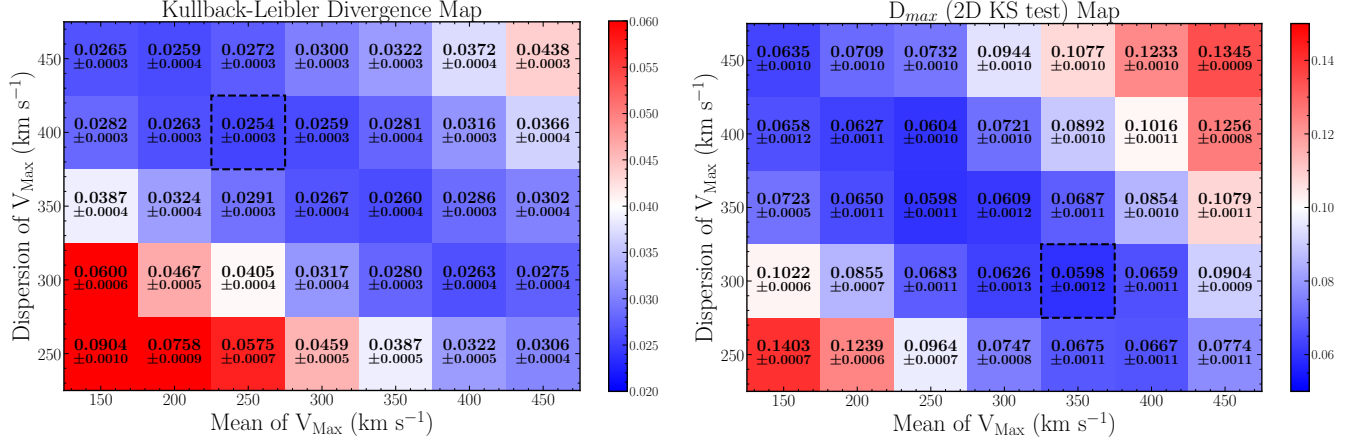


Figure 5. Left: KL divergence values for differently assumed PDFs of the launching velocity V_{\max} , while keeping the opening angle distribution fixed to its best-fit value. The Gaussian parameters (mean and standard deviation) for V_{\max} are varied and truncated below 100 km s^{-1} . The minimum KL divergence is found at a mean of 250 km s^{-1} and a standard deviation of 400 km s^{-1} . Right: same plot but showing D_{\max} values instead of KL divergence. In this case, the minimum occurs at a mean of 350 km s^{-1} and a standard deviation of 300 km s^{-1} . In each panel, the location of the lowest value is highlighted by a dashed-line box.

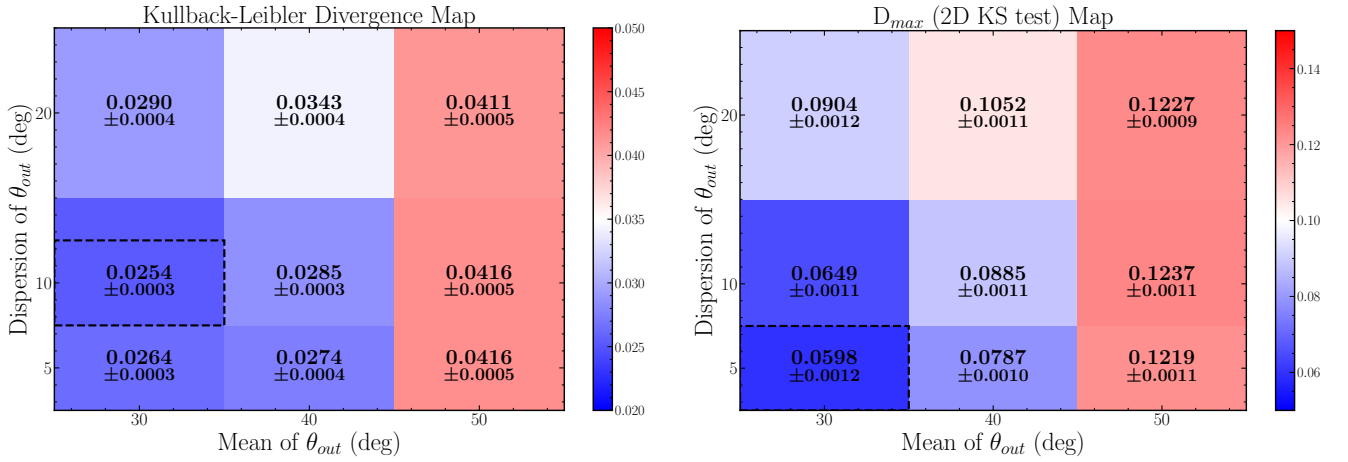


Figure 6. Left: KL divergence values computed for differently assumed PDFs of the opening angle θ_{out} . The minimum KL divergence is found when the mean and standard deviation are 30° and 10° , respectively. Right: Same as left, but showing the D_{\max} values from the 2D KS test. The minimum occurs at a mean of 30° and a standard deviation of 5° . In each panel, the location of the lowest value is highlighted by a dashed-line box.

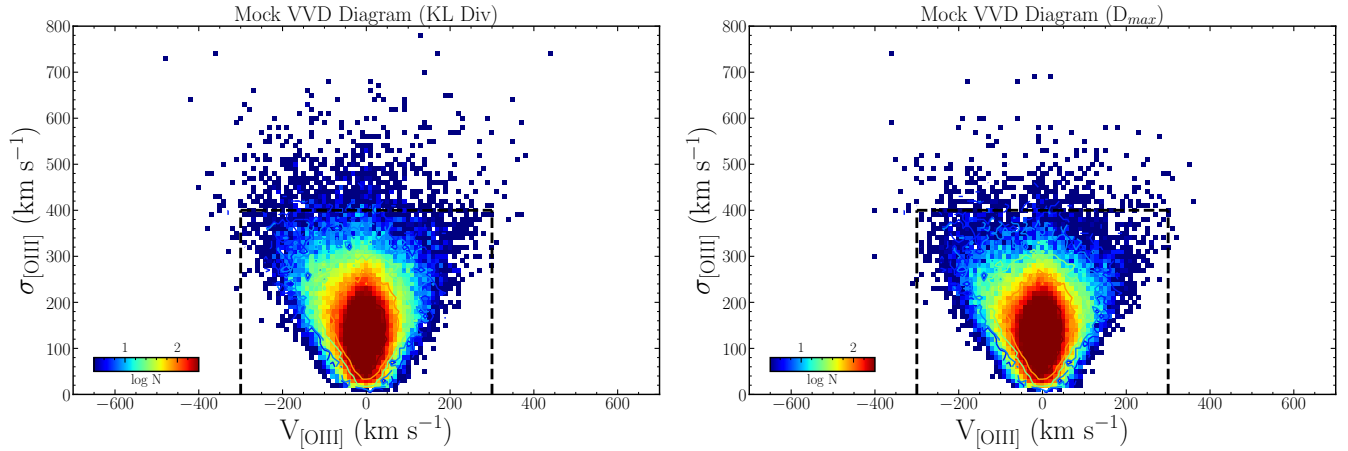


Figure 7. Best-match mock VVD distributions selected based on KL divergence (left) and D_{max} (right). The contours from the observed VVD distribution are overlaid for comparison. The dashed-box outlines the selection criterion for “strong outflow” AGNs, defined as $|V_{[OIII]}| > 300 \text{ km s}^{-1}$ or $\sigma_{[OIII]} > 400 \text{ km s}^{-1}$.

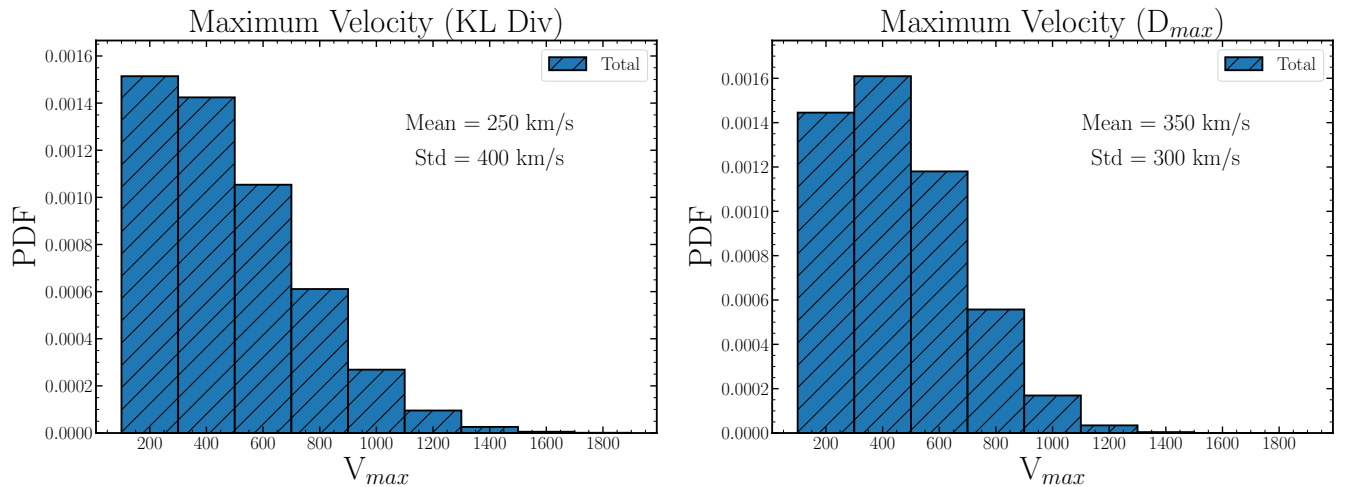


Figure 8. Best-fitting PDFs of the launching velocity based on the KL divergence (left) and D_{max} (right). Histograms show the adopted Gaussian PDFs for the full mock VVD distributions with truncation at 100 km s^{-1} . The mean and standard deviation of each Gaussian are indicated in their respective panels.

the angular outflow size becomes smaller than the seeing, leading to a significant overestimation of the outflow size even after quadratically subtracting the seeing size. Note that the measured size is also several times larger than the HWHM of the seeing size, as the seeing profile does not converge to zero even outside the FWHM. For example, if an outflow is unresolved, its seeing-convolved flux will follow the seeing profile. Thus, the outflow flux broadens the line profile at a radius further than the HWHM of the seeing, although its emission is dimmed by more than half compared to the center.

These results indicate that the seeing effect has to be carefully considered for interpreting IFU observations, i.e., initial plateau and outflow size. While the outflow size measured based on the emission line width is reliable

when the seeing size is relatively small, the outflow size can be overestimated when the seeing size is similar to or larger than the angular size of the outflow.

5. DISCUSSION

5.1. Comparison with Other Outflow Models

In this section, we discuss the characteristics of our model in comparison with the previous models developed over the last two decades. First, early outflow models did not include a rotating disk. For example, D. M. Crenshaw & S. B. Kraemer (2000); D. M. Crenshaw et al. (2000) constructed a hollow bicone model to reproduce position-velocity (PV) diagrams of nearby AGNs (e.g., V. Das et al. 2005, 2006). Subsequently, D. M. Crenshaw et al. (2010a,b) added a dust extinc-

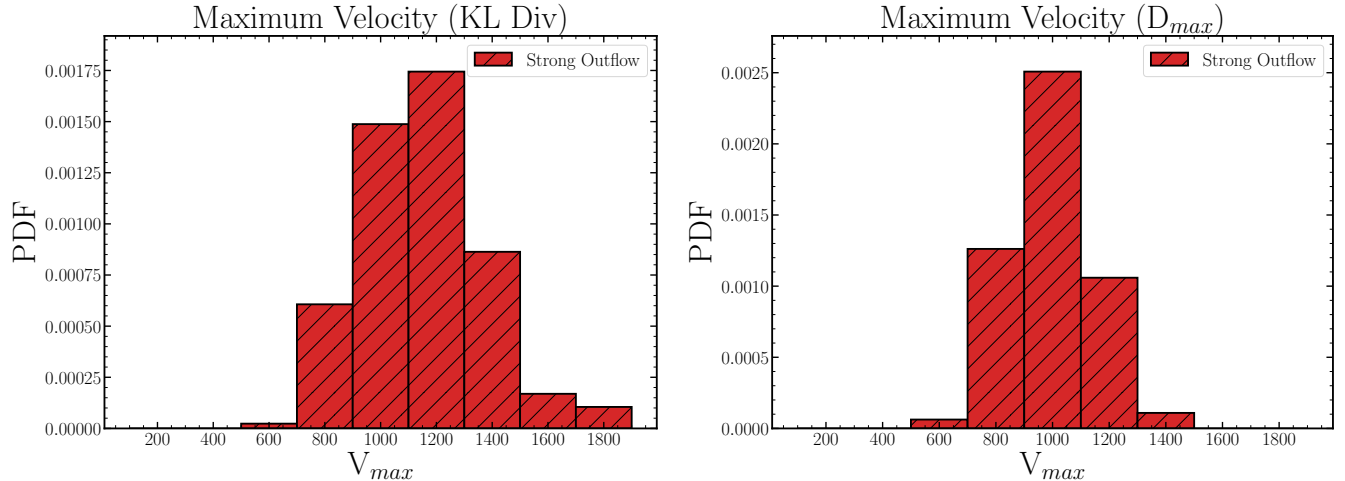


Figure 9. Distributions of the launching velocity for a subsample of strong-outflow AGNs (those lying outside the dashed boxes in Figure 7). Histograms are derived from the best-matching mock VVD distributions based on KL divergence (left) and D_{max} (right).

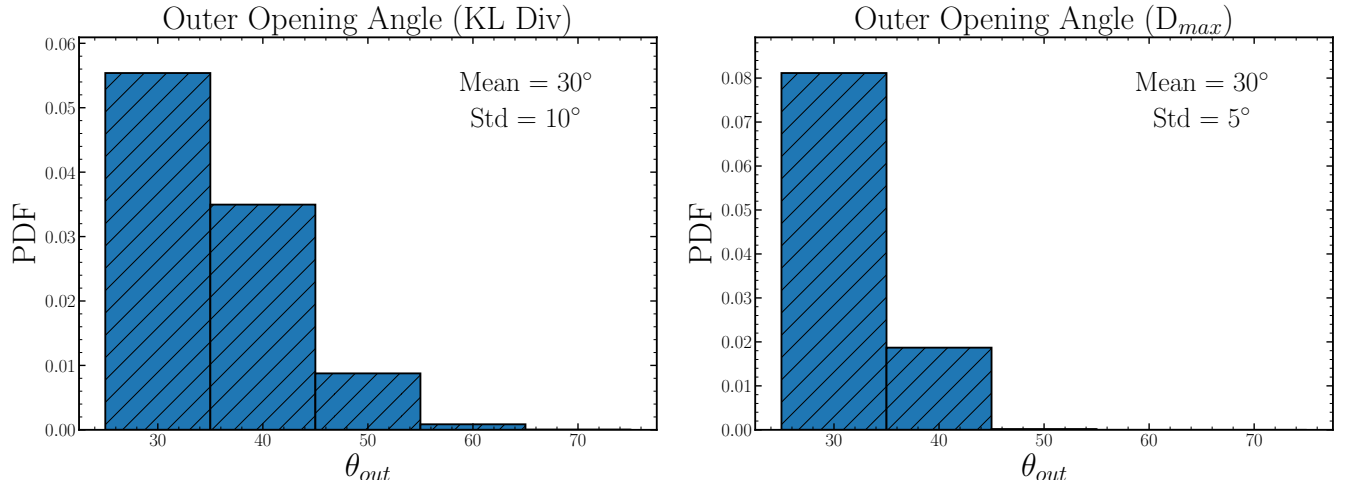


Figure 10. Best-fit PDFs for the outflow opening angle (θ_{out}) based on the KL divergence (left) and D_{max} (right). All distributions are truncated Gaussians defined over the range 30° – 70° .

tion component to the model to apply for dozens of nearby AGNs (e.g., T. C. Fischer et al. 2010, 2011, 2013; B. Meena et al. 2021; J. Falcone et al. 2024). Since these models were developed for the HST observations of nearby AGNs, it is not essential to include the effect of the point spread function (PSF).

On the other hand, S. Carniani et al. (2015) developed a model with a single approaching cone for testing their spectroastrometric analysis of powerful outflows in quasars at cosmic noon. Since the seeing effect is substantial for their high- z AGNs, they convolved each velocity channel map with the PSF, reproducing consistent [O III] flux, velocity, and velocity dispersion maps with the observations. Although their model lacks a disk

component, the contribution of the disk component is presumably weak in these extremely luminous AGNs.

Second, other models were also reported for accommodating various kinematical considerations. For example, F. Müller-Sánchez et al. (2011) constructed a model to analyze the coronal line regions (CLRs) using AO-assisted near-infrared IFU data. By combining a bi-cone model with a rotating disk, they successfully fitted CLR kinematics at the central several hundred pc, while no seeing effect was included.

Recently, C. Marconcini et al. (2023) developed a new model (MOKA^{3D}) based on G. Venturi et al. (2017) by constructing a 3D distribution of point-like clouds to reproduce the observed IFU data. The model also convolves the 3D data and assigns a proper weight to each cloud.

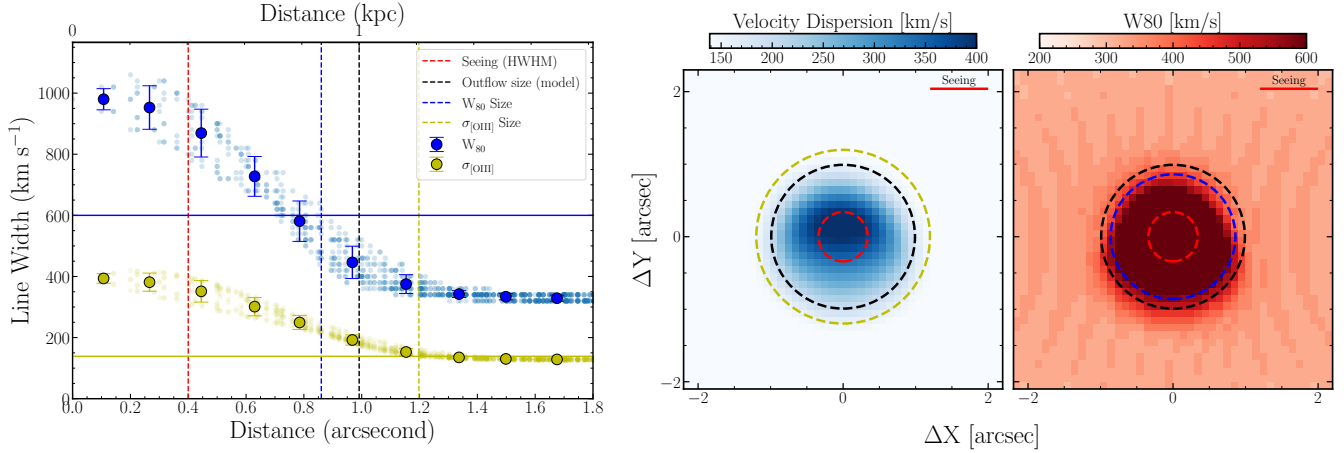


Figure 11. Example of mock IFU-analysis result for an AGN at $z = 0.05$. Left: Radial profiles of $\sigma_{\text{[OIII]}}$ (yellow markers) and W_{80} (blue markers). Large colored symbols indicate the mean velocity widths within individual radial bins. Horizontal lines mark the outflow-region criteria: $W_{80} = 600 \text{ km s}^{-1}$ (blue) and $\sigma_{\text{[OIII]}} = \sigma_*$ (yellow). Vertical dashed lines denote, from left to right, the half-width at half-maximum (HWHM) seeing size (red), the input outflow radius (black), the W_{80} -based outflow size (blue), and the $\sigma_{\text{[OIII]}}$ -based size (yellow). Right: 2D maps of velocity dispersion and W_{80} , with dashed circles following the same color scheme as the vertical lines in the left panel.

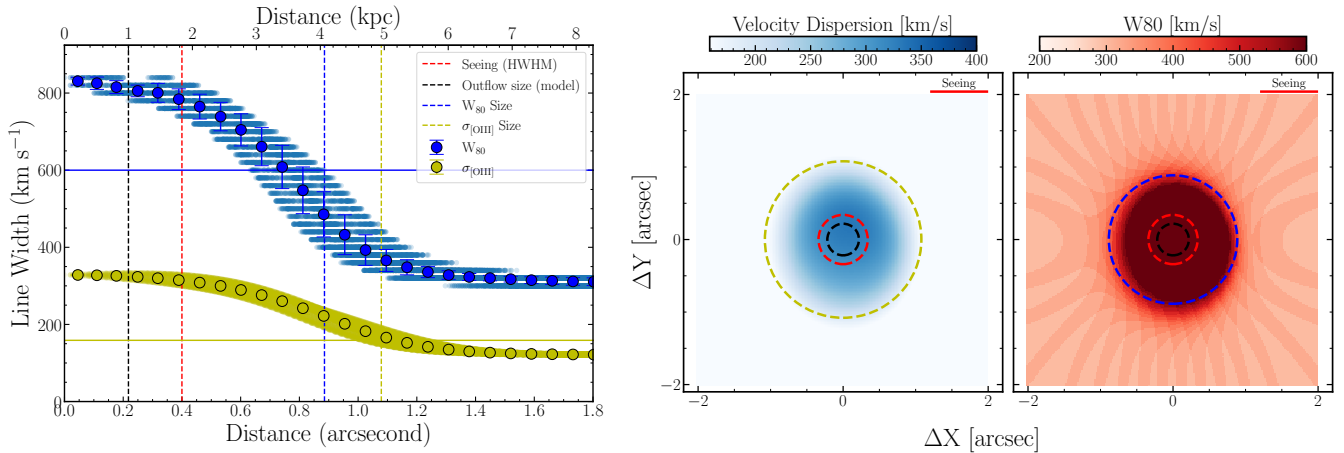


Figure 12. Same as Figure 11 but for a higher redshift of $z = 0.3$.

Since outflows often exhibit clumpy regions within their bicone geometry (e.g., D. Kakkad et al. 2023), their model has a major advantage in reproducing various substructures, showing excellent agreements with the observations of both nearby and high- z AGNs (G. Cresci et al. 2023; C. Marconcini et al. 2023, 2025a,b).

Compared to the previous models, which are mainly focused on fitting 3D data cubes of individual AGNs, our model is better suited for investigating the distributions of outflow parameters for a large sample, including the effect of seeing size and the disk component. Note that our model can also be utilized for reproducing the observation of individual AGNs (e.g., J. Shin et al. 2019). Thus, our analysis with the modified model is complementary to the previous outflow models.

5.2. Constraints on the AGN-driven outflows

The launching velocity is the key parameter for quantifying outflow energetics (see Section 5.4), while the opening angle is related to how strongly gas outflows interact with the ISM. Thus, it is essential to constrain the launching velocity and opening angle of outflows for a large sample to investigate AGN feedback.

We report launching velocities of $\lesssim 1500 \text{ km s}^{-1}$ and typical opening angles of 30° - 40° (Section 4.2). For a consistency check, we discuss the previous estimations of these two parameters, mostly from nearby AGNs. For example, D. M. Crenshaw & S. B. Kraemer (2000); D. M. Crenshaw et al. (2000) reported the inner/outer opening angles as $26^\circ/40^\circ$ and the maximum outflow velocity as 1300 km s^{-1} for NGC 1068, and inner/outer

opening angles as $20^\circ/36^\circ$ and the maximum outflow velocity as 750 km s^{-1} for NGC 4151 (see also V. Das et al. 2005, 2006). After including dust extinction, the outer opening angles are slightly changed to 40° for NGC 1068 and 33° for NGC 4151 (D. M. Crenshaw et al. 2010b).

Their following studies also reported outflow parameters of other nearby AGNs (D. M. Crenshaw et al. 2010a; T. C. Fischer et al. 2010, 2011; B. Meena et al. 2021; J. Falcone et al. 2024). In particular, among the cases of 17 Seyfert galaxies investigated by T. C. Fischer et al. (2013), the maximum velocity agrees with our range of $V_{max} \leq 1500 \text{ km s}^{-1}$, except for NGC 1068. On the other hand, the outer opening angle distribution is slightly different. While a majority of their sample shows consistent opening angles ($<50^\circ$) with our results, 7 AGNs have wider opening angles. The difference can be caused by a couple of effects. First, AGNs with higher luminosity and stronger outflows are likely to have wider opening angles (H.-J. Bae & J.-H. Woo 2016). For example, only 13% of our type 2 AGN sample have bolometric luminosity higher than $10^{44.5} \text{ erg/s}$, while more than half of their sample (9/17) are more luminous than $10^{44.5} \text{ erg/s}$. Second, their sample was selected based on clear signs of extended outflows, whereas we do not apply any criterion on the outflow extent. The inclusion of the disk component in our model can also induce differences.

J. Shin et al. (2019) also simulated 2D flux, velocity, and velocity dispersion maps of NGC 5728 by adding seeing convolution to the H.-J. Bae & J.-H. Woo (2016) model. The outer half opening angle was estimated as 28° , which is the most prevalent value in our best PDFs. In contrast, M. Durré & J. Mould (2019) constrained the projected full opening angle to 71° based on [Fe II] $1.644 \mu\text{m}$ line. As discussed in J. Shin et al. (2019), this discrepancy may originate from different analytic models between the two studies.

The maximum velocity and the outer opening angle estimated by F. Müller-Sánchez et al. (2011, 2016) are also consistent with our constraints. On the other hand, for the best-fit parameters from R. Nevin et al. (2018), while the maximum velocities ($V_{max} = 230 - 720 \text{ km s}^{-1}$) also agree with our study, most of the opening angle values are much higher than the typical range of our constraint. This discrepancy also appears to be due to different biconical model and/or the characteristics of their sample (i.e., AGNs with double-peaked narrow emission lines). Other studies that constrained the opening angles of individual galaxies (e.g., D. Baron et al. 2018; R. A. Riffel 2021; J. H. Costa-Souza et al. 2024) are in agreement with our constraint.

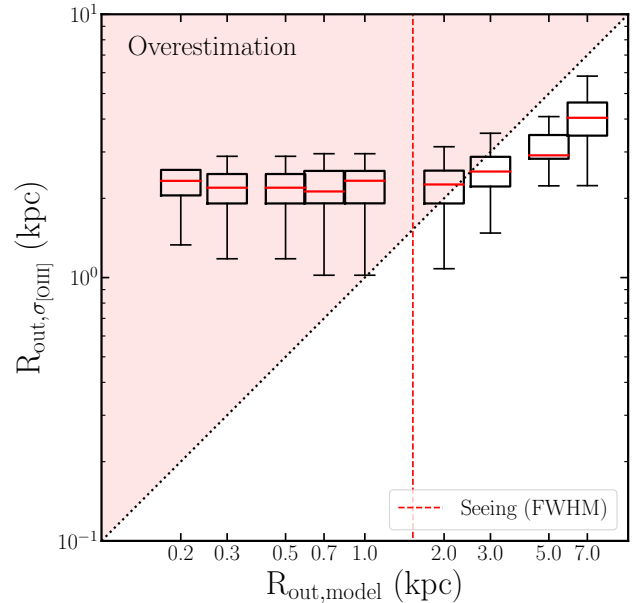


Figure 13. Comparison between the measured outflow sizes based on $\sigma_{\text{[OIII]}}$ and the input outflow sizes. The red vertical line indicates the seeing (FWHM= $0.8'' \sim 1.52 \text{ kpc}$ at $z=0.1$) while the black dotted line shows a one-to-one relation.

5.3. True Outflow Size

In Section 4.3, we verified that the outflow size measured based on velocity widths can be significantly overestimated by the seeing, especially when a true outflow size is comparable to or smaller than the seeing size. To properly constrain the spatial scale of outflows, it is essential to investigate the seeing-limited cases in detail.

Previous studies reported notable spatial features in luminous type 2 AGNs, i.e., circularly extended NLR morphologies or enhanced W_{80} values with flat radial profiles (e.g., G. Liu et al. 2013a,b; C. M. Harrison et al. 2014). Interestingly, our model reproduces a similar flat W_{80} profile when the outflow is compact and the disk emission is much weaker than the outflow. Seeing convolution of a compact outflow generates a broad wing component with an almost constant velocity width across the entire FoV, while the disk emission is too faint to affect the velocity width, even at pixels far from the center. Thus, given that their samples consist of luminous type 2 quasars, implying relatively weak disk emission, the flat W_{80} profiles may indicate smaller outflow sizes.

Furthermore, M. Villar-Martín et al. (2016) found that only 2 out of 15 AGNs in their sample show clearly resolved outflows by comparing the spatial profiles of seeing with the [O III] wing emission. Based on spectroastrometry and seeing sizes, they constrained lower and upper limits of the outflow sizes as several hundred pc and a few kpc, respectively. These results are in

agreement with our constraints and represent observational evidence of the seeing effect in local AGNs.

For type 1 AGNs, the BLR emission (mostly $H\beta$) can serve as a reference PSF for deblending methods (B. Husemann et al. 2013, 2014, 2016; H. Ibarra-Medel et al. 2025). For example, B. Husemann et al. (2013) reported that a significant fraction of their type 1 AGN sample shows no/weak extended emission after a PSF subtraction. They also found that the resolved [O III] component often exhibits a significantly narrower velocity width, indicating no extended outflows. Despite the effectiveness of their method, it cannot be applied to type 2 AGNs since it requires a reference PSF from BLR emission. In addition, a compact but extended outflow can remain even after a PSF subtraction, leading to an overestimation of the size.

M. Singha et al. (2022) tested whether the [O III] wing component is spatially resolved for type 1 AGNs at $z < 0.06$ by comparing the 2D flux map with a PSF from the broad $H\beta$, finding that 23 out of 36 AGNs show unresolved [O III] wing components. They also reported a median spatial offset of ~ 27 pc between the center of AGN and flux centroid of [O III] wing component for the unresolved cases, which can be considered as lower limits of the outflow size. In contrast, based on the $\sigma_{[\text{O III}]}$ -based method of M. Karouzos et al. (2016), they obtained an order of magnitude larger sizes than their lower limits, suggesting that the seeing effect can significantly overestimate the outflow sizes.

In our previous IFU studies (M. Karouzos et al. 2016; H.-J. Bae et al. 2017; D. Kang & J.-H. Woo 2018; R. Luo et al. 2021; C. Kim et al. 2023), the outflow sizes were determined based on the $\sigma_{[\text{O III}]}$ -based method. Our main conclusion was that the outflow sizes are mostly less than several kpc scales, indicating a lack of galactic scale feedback. We also reported a kinematic outflow size–luminosity relation between the outflow size and the [O III] luminosity with a slope of ~ 0.3 . For this work, we subtracted the HWHM of the seeing size from the outflow size in quadrature to correct for the seeing effect. However, this correction may not be sufficient as shown in Section 4.3. Thus, our measurements can be conservatively considered as upper limits, particularly for higher redshift targets among our sample ($z > 0.1$).

To test the reliability of the size measurements, we apply the $\sigma_{[\text{O III}]}$ -based method to various mock data. For this test, we set the redshift $z=0.1$ as a representative case and restrict V_{max} from 750 to 2000 km s^{-1} to focus on strong outflows (see Section 4.2). In Figure 13, we present the measured outflow size as a function of the input (true) size. As expected, the outflow size is overestimated by more than a factor of two when the true

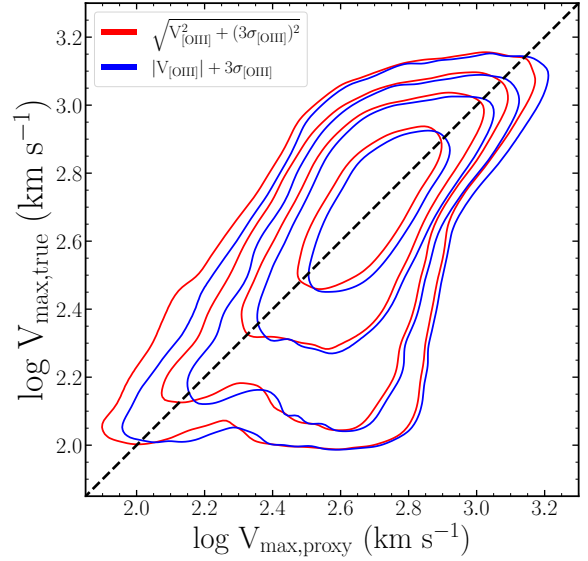


Figure 14. Comparison of the launching velocity with its proxies derived from mock kinematics in the MC simulation. The red and blue contours show 0.5 - 2 σ levels when we use a quadratic sum ($\sqrt{V_{[\text{O III}] }^2 + (3\sigma_{[\text{O III}]})^2}$) (H.-J. Bae & J.-H. Woo 2016) and a direct summation ($|V_{[\text{O III}] }| + 3\sigma_{[\text{O III}]}$) (D. S. N. Rupke & S. Veilleux 2013) as a proxy, respectively. The dashed line indicates a one-to-one relation.

outflow size is smaller than the FWHM of the seeing (~ 1.52 kpc at $z = 0.1$). On the other hand, when the seeing is smaller than the true size, the measured size is generally consistent with the input size with slight underestimations (< 0.3 dex). Therefore, the $\sigma_{[\text{O III}]}$ -based method provides a good size estimation within 0.3 dex, or at least can be used as a reliable upper limit, depending on the relative seeing size.

We emphasize that although the $\sigma_{[\text{O III}]}$ -based method overestimates the sizes of compact outflows, the main conclusion of C. Kim et al. (2023), i.e., lack of global feedback, remains valid. Since the true size can be more compact than the measured one, the upper limit of the size still provides strong constraints on the spatial scales of AGN feedback.

It is also noteworthy that the measured sizes are broadly consistent within ~ 0.3 dex at a given input size, regardless of other input parameters. There are some outliers with small measured sizes, which mostly have slow launching velocities (< 1000 km s^{-1}). Thus, if the launching velocity is fast enough, the $\sigma_{[\text{O III}]}$ -based size has no significant dependence on other parameters.

5.4. Outflow Energetics

In this section, we present estimates of the mass outflow rate (\dot{M}_{out}), momentum rate (\dot{P}_{out}), and kinetic power (\dot{E}_{out}) for local type 2 AGNs to assess the ef-

efficiency of AGN feedback. For conical outflows, these quantities are computed as (e.g., R. Maiolino et al. 2012; F. Fiore et al. 2017)

$$\dot{M}_{\text{out}} = 3 M_{\text{out}} \frac{v_{\text{out}}}{R_{\text{out}}}, \quad (9)$$

$$\dot{P}_{\text{out}} = \dot{M}_{\text{out}} v_{\text{out}}, \quad (10)$$

$$\dot{E}_{\text{out}} = \frac{1}{2} \dot{M}_{\text{out}} v_{\text{out}}^2, \quad (11)$$

where M_{out} , v_{out} , and R_{out} denote the ionized gas mass, outflow velocity, and outflow size, respectively. We estimate the ionized gas mass from the extinction-corrected [O III] luminosity using Eq. 29 of S. Veilleux et al. (2020), adopting a fixed electron density of 1000 cm^{-3} .

A variety of velocity definitions have been used in previous studies to approximate the characteristic outflow velocity, including W_{80} (e.g., D. Wylezalek et al. 2020; D. Ruschel-Dutra et al. 2021), $\sqrt{v_{[\text{OIII}]}^2 + \sigma_{[\text{OIII}]}^2}$ (e.g., S. Rakshit & J.-H. Woo 2018; C. Kim et al. 2023), and $v_{\text{broad}} + 2\sigma_{\text{broad}}$ (e.g., D. S. N. Rupke & S. Veilleux 2013; F. Fiore et al. 2017). In our analysis, we derive a mass-weighted mean outflow velocity based on the radial profiles of the intrinsic velocity ($v(R) = V_{\text{max}}(1 - R/R_{\text{out}})$) and flux ($f(R) = f_0 e^{-5R/R_{\text{out}}}$) in our model, assuming an electron density profile $n_e(R) \propto R^{-2}$. Since the mass is proportional to $L_{[\text{OIII}]} / n_e$, the mass-weighted mean velocity becomes

$$\begin{aligned} v_{\text{out}} &= \frac{\int_0^{R_{\text{out}}} v(R) M_{\text{out}}(R) R^2 dR}{\int_0^{R_{\text{out}}} M_{\text{out}}(R) R^2 dR} \\ &= \frac{\int_0^{R_{\text{out}}} V_{\text{max}} \left(1 - \frac{R}{R_{\text{out}}}\right) f_0 e^{-5R/R_{\text{out}}} n_e^{-1}(R) R^2 dR}{\int_0^{R_{\text{out}}} f_0 e^{-5R/R_{\text{out}}} n_e^{-1}(R) R^2 dR} \\ &= V_{\text{max}} \frac{\int_0^1 t^4 (1-t) e^{-5t} dt}{\int_0^1 t^4 e^{-5t} dt} \simeq 0.31 V_{\text{max}}. \end{aligned} \quad (12)$$

Thus, the mass-weighted mean outflow velocity is approximately $v_{\text{out}} = 0.31 V_{\text{max}}$. Since the momentum and kinetic power scale with v_{out}^2 and v_{out}^3 , respectively, their mass-weighted mean values correspond to $\sim 0.14 V_{\text{max}}^2$ and $\sim 0.07 V_{\text{max}}^3$. These relations are used to calculate \dot{M}_{out} , \dot{P}_{out} , and \dot{E}_{out} .

Note that the launching velocity cannot be directly measured from observational data. Instead, we test several potential proxies for V_{max} that can be computed from the observed $V_{[\text{OIII}]}$ and $\sigma_{[\text{OIII}]}$, using the mock SDSS sample (Section 4.2). We find that two commonly used prescriptions show good agreement with the input V_{max} . The first is the quadratic sum of $|V_{[\text{OIII}]}|$ and $3\sigma_{[\text{OIII}]}$, similar to that adopted by H.-J. Bae & J.-H.

Woo (2016) and J. Rodríguez Zaurín et al. (2013). The second is the direct sum $|V_{[\text{OIII}]}| + 3\sigma_{[\text{OIII}]}$, following D. S. N. Rupke & S. Veilleux (2013) and F. Fiore et al. (2017). Figure 14 demonstrates that both proxies recover the launching velocity with a scatter of ~ 0.2 dex. In the following analysis, we adopt the first proxy (i.e., the quadratic sum).

Lastly, we use two different outflow size estimates to set upper and lower limits on the energetics. First, we adopt the $\sigma_{[\text{OIII}]}$ -based sizes inferred from the kinematic outflow size–luminosity relation as upper limits (see Section 5.3), and compute the corresponding lower limits on the outflow rates. Second, we employ the NLR sizes from the NLR size–luminosity relation derived for nearby AGNs (G. E. Polack et al. 2024). We convert these NLR sizes to outflow sizes by dividing by three, following the typical ratio of $R_{\text{out}}/R_{[\text{OIII}]}$ reported in T. C. Fischer et al. (2018) and G. E. Polack et al. (2024), and then calculate the corresponding upper limits on the outflow rates. These NLR-based sizes are typically 0.4–0.6 dex smaller than the $\sigma_{[\text{OIII}]}$ -based sizes in the dynamic range of the [O III] luminosity.

In Figure 15, we compare the upper and lower limits of the outflow rates as a function of the bolometric luminosity to evaluate whether the outflows are sufficiently energetic to drive efficient feedback. Despite the large scatter, the estimated outflow rates (shown as contours) generally fall within the ranges $\dot{M}_{\text{out}} \sim 1\text{--}100 L_{\text{bol}}/\eta c^2$ ($\eta = 0.1$), $\dot{P}_{\text{out}} \sim 0.01\text{--}1 L_{\text{bol}}/c$, and $\dot{E}_{\text{out}} \sim 10^{-6}\text{--}10^{-3} L_{\text{bol}}$. These ranges are broadly consistent with previous studies, though some systematic differences arise from the various definitions adopted for outflow parameters. For instance, the F. Fiore et al. (2017) sample reports kinetic powers typically in the range of 0.01–1% of L_{bol} , largely because their characteristic outflow velocity is defined using the broad [O III] component ($|v_{\text{broad}}| + 2\sigma_{\text{broad}}$), which yields substantially larger v_{out} values. By contrast, our analysis computes v_{out} from the first and second moments of the total [O III] line profile, resulting in systematically smaller velocities at fixed luminosity. This discrepancy becomes even more pronounced in \dot{E}_{out} , as the kinetic power scales with v_{out}^3 .

Theoretical studies generally suggest that the kinetic power of AGN-driven outflows is required to be 0.5–5% of the bolometric luminosity for efficient AGN feedback (e.g., T. Di Matteo et al. 2005; P. F. Hopkins et al. 2008; K. Zubovas & A. King 2012). Our estimated kinetic powers are mostly much lower than this threshold, indicating that the feedback may not be efficient for the bulk of the sample. It is important to note, however, that our estimates are based solely on the ionized gas component,

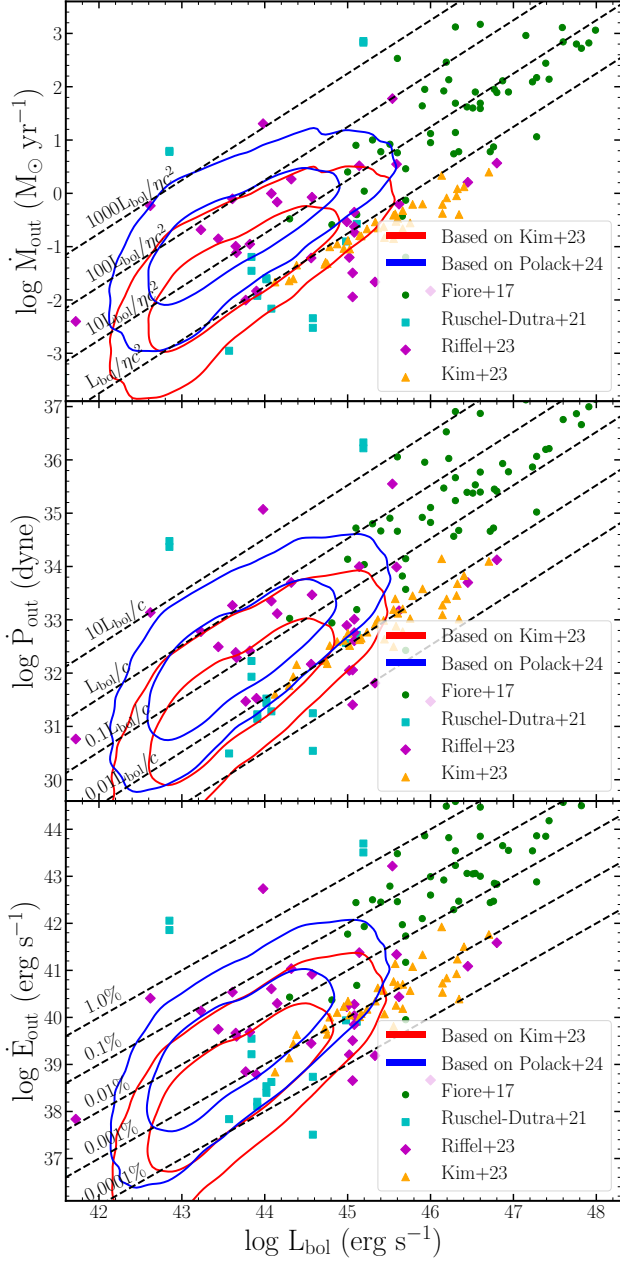


Figure 15. Mass outflow rate ($\log \dot{M}_{\text{out}}$, top), momentum rate ($\log \dot{P}_{\text{out}}$, middle), and kinetic power ($\log \dot{E}_{\text{out}}$, bottom) as a function of the bolometric luminosity of the SDSS type 2 AGNs. The red and blue contours show the energetics based on the upper limits (red contours) and lower limits (blue contours) of the outflow sizes. The energetics of individual AGNs from the literature are denoted with various symbols.

which represents only a small fraction of the total outflow mass (e.g., A. Fluetsch et al. 2019). Nevertheless, a non-negligible subset of AGNs—0.85% or 0.14% depending on whether the outflow sizes are estimated using the G. E. Polack et al. (2024) or C. Kim et al. (2023) relations, respectively—exhibits $\dot{E}_{\text{out}}/L_{\text{bol}} > 0.5\%$. These

AGNs also show high outflow velocities, making them excellent targets for spatially resolved outflow studies in detail.

5.5. Limitations of the current model

Despite these improvements, our model and mock data analysis still have several limitations. First, because we adopt analytic functions for the flux and velocity distributions, the model cannot capture the detailed substructures of real outflows. High-resolution studies of nearby AGNs have revealed clumpy and irregular features within the bicone (e.g., G. Venturi et al. 2018; M. Mingozzi et al. 2019; D. Kakkad et al. 2023), which are not represented in our simplified prescription.

Second, our mock data do not include flux uncertainties. For instance, the $\sigma_{[\text{O III}]}$ -based method defines the outflow size as the radius of the outermost [O III]-detected pixel when the $\sigma_{[\text{O III}]}/\sigma_*$ does not converge to unity; in such cases, the S/N becomes critical in determining the size. We also did not test spectroastrometry-based techniques (e.g., S. Carniani et al. 2015; M. Singha et al. 2022), which estimate the outflow size from the spatial offset between the center and the flux centroid of the [O III] emission. These methods require realistic flux errors to properly fit the 2D flux distribution and determine the centroid.

Third, we assume that all parameter PDFs in the MC simulations are independent, owing to the lack of well-established relations among them. In reality, several outflow parameters are expected to be correlated, implying that multivariate PDFs may be more appropriate. Previous studies have reported correlations between outflow properties and bolometric luminosity (or Eddington ratio). The opening angle and outflow velocity are also suggested to have positive (H.-J. Bae & J.-H. Woo 2016), negative (F. Müller-Sánchez et al. 2011), or no correlations (T. C. Fischer et al. 2013). Future MC simulations incorporating such parameter correlations may better reproduce the observed gas kinematics.

6. SUMMARY

In this study, we present the modified outflow model and its applications to local type 2 AGNs. Here we summarize the main results of this study.

1. We find that including a rotating disk component in the model reduces the gas velocity and velocity dispersion within the SDSS fiber size. Thus, the outflow launching velocity needs to be faster to compensate for the disk contribution. The observed VVD distribution of the local type 2 AGNs can be reproduced by $V_{\text{max}} \lesssim 1500 \text{ km s}^{-1}$.

2. Based on the MC simulations to reproduce the observed VVD distribution, we find that the launching velocity is $\lesssim 1000 \text{ km s}^{-1}$ for a majority of the type 2 AGNs except for several percent of strong outflow cases ($> 1000 - 1500 \text{ km s}^{-1}$), and that the outer half opening angle is less than 50° .
3. By generating mock IFU data, we find similar features reported in previous IFU studies, e.g., circular morphology in the flux map and the initial plateau of the radial profiles of velocity widths. These results suggest that the biconical model with a seeing convolution can successfully reproduce observational data.
4. By investigating the seeing effect on the outflow size measurement, we confirmed that the outflow

size measured based on velocity widths can be overestimated, particularly when the angular size of the outflow is comparable to or smaller than the seeing size. Nevertheless, this still supports the lack of global feedback since the previously reported sizes can be considered as upper limits.

ACKNOWLEDGMENTS

This work has been supported by the Basic Science Research Program through the National Research Foundation of the Korean Government (2021R1A2C3008486).

Software: astropy (Astropy Collaboration et al. 2022), matplotlib (J. D. Hunter 2007), numpy (C. R. Harris et al. 2020), scipy (P. Virtanen et al. 2020)

REFERENCES

- Amorisco, N. C., & Bertin, G. 2010, A&A, 519, A47, doi: [10.1051/0004-6361/201014387](https://doi.org/10.1051/0004-6361/201014387)
- Astropy Collaboration, Price-Whelan, A. M., Lim, P. L., et al. 2022, ApJ, 935, 167, doi: [10.3847/1538-4357/ac7c74](https://doi.org/10.3847/1538-4357/ac7c74)
- Bae, H.-J., & Woo, J.-H. 2016, ApJ, 828, 97, doi: [10.3847/0004-637X/828/2/97](https://doi.org/10.3847/0004-637X/828/2/97)
- Bae, H.-J., Woo, J.-H., Karouzos, M., et al. 2017, ApJ, 837, 91, doi: [10.3847/1538-4357/aa5f5c](https://doi.org/10.3847/1538-4357/aa5f5c)
- Baron, D., Netzer, H., Prochaska, J. X., et al. 2018, MNRAS, 480, 3993, doi: [10.1093/mnras/sty2113](https://doi.org/10.1093/mnras/sty2113)
- Boroson, T. 2005, AJ, 130, 381, doi: [10.1086/431722](https://doi.org/10.1086/431722)
- Bouché, N., Carfantan, H., Schroetter, I., Michel-Dansac, L., & Contini, T. 2015, AJ, 150, 92, doi: [10.1088/0004-6256/150/3/92](https://doi.org/10.1088/0004-6256/150/3/92)
- Carniani, S., Marconi, A., Maiolino, R., et al. 2015, A&A, 580, A102, doi: [10.1051/0004-6361/201526557](https://doi.org/10.1051/0004-6361/201526557)
- Costa-Souza, J. H., Riffel, R. A., Dors, O. L., Riffel, R., & da Rocha-Poppe, P. C. 2024, MNRAS, 527, 9192, doi: [10.1093/mnras/stad3809](https://doi.org/10.1093/mnras/stad3809)
- Crenshaw, D. M., & Kraemer, S. B. 2000, ApJL, 532, L101, doi: [10.1086/312581](https://doi.org/10.1086/312581)
- Crenshaw, D. M., Kraemer, S. B., Schmitt, H. R., et al. 2010a, AJ, 139, 871, doi: [10.1088/0004-6256/139/3/871](https://doi.org/10.1088/0004-6256/139/3/871)
- Crenshaw, D. M., Schmitt, H. R., Kraemer, S. B., Mushotzky, R. F., & Dunn, J. P. 2010b, ApJ, 708, 419, doi: [10.1088/0004-637X/708/1/419](https://doi.org/10.1088/0004-637X/708/1/419)
- Crenshaw, D. M., Kraemer, S. B., Hutchings, J. B., et al. 2000, AJ, 120, 1731, doi: [10.1086/301574](https://doi.org/10.1086/301574)
- Cresci, G., Tozzi, G., Perna, M., et al. 2023, A&A, 672, A128, doi: [10.1051/0004-6361/202346001](https://doi.org/10.1051/0004-6361/202346001)
- Das, V., Crenshaw, D. M., Kraemer, S. B., & Deo, R. P. 2006, AJ, 132, 620, doi: [10.1086/504899](https://doi.org/10.1086/504899)
- Das, V., Crenshaw, D. M., Hutchings, J. B., et al. 2005, AJ, 130, 945, doi: [10.1086/432255](https://doi.org/10.1086/432255)
- Deconto-Machado, A., Riffel, R. A., Ilha, G. S., et al. 2022, A&A, 659, A131, doi: [10.1051/0004-6361/202140613](https://doi.org/10.1051/0004-6361/202140613)
- Di Matteo, T., Springel, V., & Hernquist, L. 2005, Nature, 433, 604, doi: [10.1038/nature03335](https://doi.org/10.1038/nature03335)
- Durré, M., & Mould, J. 2019, ApJ, 870, 37, doi: [10.3847/1538-4357/aaf000](https://doi.org/10.3847/1538-4357/aaf000)
- Dutton, A. A., van den Bosch, F. C., Faber, S. M., et al. 2011, MNRAS, 410, 1660, doi: [10.1111/j.1365-2966.2010.17555.x](https://doi.org/10.1111/j.1365-2966.2010.17555.x)
- Fabian, A. C. 2012, ARA&A, 50, 455, doi: [10.1146/annurev-astro-081811-125521](https://doi.org/10.1146/annurev-astro-081811-125521)
- Falcone, J., Crenshaw, D. M., Fischer, T. C., et al. 2024, ApJ, 971, 17, doi: [10.3847/1538-4357/ad5283](https://doi.org/10.3847/1538-4357/ad5283)
- Fiore, F., Feruglio, C., Shankar, F., et al. 2017, A&A, 601, A143, doi: [10.1051/0004-6361/201629478](https://doi.org/10.1051/0004-6361/201629478)
- Fischer, T. C., Crenshaw, D. M., Kraemer, S. B., & Schmitt, H. R. 2013, ApJS, 209, 1, doi: [10.1088/0067-0049/209/1/1](https://doi.org/10.1088/0067-0049/209/1/1)
- Fischer, T. C., Crenshaw, D. M., Kraemer, S. B., et al. 2011, ApJ, 727, 71, doi: [10.1088/0004-637X/727/2/71](https://doi.org/10.1088/0004-637X/727/2/71)
- Fischer, T. C., Crenshaw, D. M., Kraemer, S. B., Schmitt, H. R., & Trippe, M. L. 2010, AJ, 140, 577, doi: [10.1088/0004-6256/140/2/577](https://doi.org/10.1088/0004-6256/140/2/577)
- Fischer, T. C., Kraemer, S. B., Schmitt, H. R., et al. 2018, ApJ, 856, 102, doi: [10.3847/1538-4357/aab03e](https://doi.org/10.3847/1538-4357/aab03e)
- Fluetsch, A., Maiolino, R., Carniani, S., et al. 2019, MNRAS, 483, 4586, doi: [10.1093/mnras/sty3449](https://doi.org/10.1093/mnras/sty3449)

- Gatto, L., Storchi-Bergmann, T., Riffel, R. A., et al. 2024, MNRAS, 530, 3059, doi: [10.1093/mnras/stae989](https://doi.org/10.1093/mnras/stae989)
- Greene, J. E., & Ho, L. C. 2005, ApJ, 627, 721, doi: [10.1086/430590](https://doi.org/10.1086/430590)
- Harris, C. R., Millman, K. J., van der Walt, S. J., et al. 2020, Nature, 585, 357, doi: [10.1038/s41586-020-2649-2](https://doi.org/10.1038/s41586-020-2649-2)
- Harrison, C. M. 2017, Nature Astronomy, 1, 0165, doi: [10.1038/s41550-017-0165](https://doi.org/10.1038/s41550-017-0165)
- Harrison, C. M., Alexander, D. M., Mullaney, J. R., & Swinbank, A. M. 2014, MNRAS, 441, 3306, doi: [10.1093/mnras/stu515](https://doi.org/10.1093/mnras/stu515)
- Harrison, C. M., & Ramos Almeida, C. 2024, Galaxies, 12, 17, doi: [10.3390/galaxies12020017](https://doi.org/10.3390/galaxies12020017)
- Hopkins, P. F., Hernquist, L., Cox, T. J., & Kereš, D. 2008, ApJS, 175, 356, doi: [10.1086/524362](https://doi.org/10.1086/524362)
- Hunter, J. D. 2007, Computing in Science & Engineering, 9, 90, doi: [10.1109/MCSE.2007.55](https://doi.org/10.1109/MCSE.2007.55)
- Husemann, B., Jahnke, K., Sánchez, S. F., et al. 2014, MNRAS, 443, 755, doi: [10.1093/mnras/stu1167](https://doi.org/10.1093/mnras/stu1167)
- Husemann, B., Scharwächter, J., Bennert, V. N., et al. 2016, A&A, 594, A44, doi: [10.1051/0004-6361/201527992](https://doi.org/10.1051/0004-6361/201527992)
- Husemann, B., Jahnke, K., Sánchez, S. F., et al. 2013, A&A, 549, A87, doi: [10.1051/0004-6361/201220582](https://doi.org/10.1051/0004-6361/201220582)
- Ibarra-Medel, H., Negrete, C. A., Lacerna, I., et al. 2025, MNRAS, 536, 752, doi: [10.1093/mnras/stae2623](https://doi.org/10.1093/mnras/stae2623)
- Kakkad, D., Mainieri, V., Vietri, G., et al. 2023, MNRAS, 520, 5783, doi: [10.1093/mnras/stad439](https://doi.org/10.1093/mnras/stad439)
- Kang, D., & Woo, J.-H. 2018, ApJ, 864, 124, doi: [10.3847/1538-4357/aad561](https://doi.org/10.3847/1538-4357/aad561)
- Karouzos, M., Woo, J.-H., & Bae, H.-J. 2016, ApJ, 819, 148, doi: [10.3847/0004-637X/819/2/148](https://doi.org/10.3847/0004-637X/819/2/148)
- Kim, C., Woo, J.-H., Luo, R., et al. 2023, ApJ, 958, 145, doi: [10.3847/1538-4357/acf92b](https://doi.org/10.3847/1538-4357/acf92b)
- Kullback, S., & Leibler, R. A. 1951, The Annals of Mathematical Statistics, 22, 79, doi: [10.1214/aoms/1177729694](https://doi.org/10.1214/aoms/1177729694)
- Liu, G., Zakamska, N. L., Greene, J. E., Nesvadba, N. P. H., & Liu, X. 2013a, MNRAS, 430, 2327, doi: [10.1093/mnras/stt051](https://doi.org/10.1093/mnras/stt051)
- Liu, G., Zakamska, N. L., Greene, J. E., Nesvadba, N. P. H., & Liu, X. 2013b, MNRAS, 436, 2576, doi: [10.1093/mnras/stt1755](https://doi.org/10.1093/mnras/stt1755)
- Luo, R., Woo, J.-H., Shin, J., et al. 2019, ApJ, 874, 99, doi: [10.3847/1538-4357/ab08e6](https://doi.org/10.3847/1538-4357/ab08e6)
- Luo, R., Woo, J.-H., Karouzos, M., et al. 2021, ApJ, 908, 221, doi: [10.3847/1538-4357/abd5ac](https://doi.org/10.3847/1538-4357/abd5ac)
- Maiolino, R., Gallerani, S., Neri, R., et al. 2012, MNRAS, 425, L66, doi: [10.1111/j.1745-3933.2012.01303.x](https://doi.org/10.1111/j.1745-3933.2012.01303.x)
- Marconcini, C., Marconi, A., Cresci, G., et al. 2023, A&A, 677, A58, doi: [10.1051/0004-6361/202346821](https://doi.org/10.1051/0004-6361/202346821)
- Marconcini, C., Feltre, A., Lamperti, I., et al. 2025a, A&A, 701, A113, doi: [10.1051/0004-6361/202554797](https://doi.org/10.1051/0004-6361/202554797)
- Marconcini, C., Marconi, A., Cresci, G., et al. 2025b, Nature Astronomy, 9, 907, doi: [10.1038/s41550-025-02518-6](https://doi.org/10.1038/s41550-025-02518-6)
- Marin, F. 2014, MNRAS, 441, 551, doi: [10.1093/mnras/stu593](https://doi.org/10.1093/mnras/stu593)
- Meena, B., Crenshaw, D. M., Schmitt, H. R., et al. 2021, ApJ, 916, 31, doi: [10.3847/1538-4357/ac0246](https://doi.org/10.3847/1538-4357/ac0246)
- Mingozzi, M., Cresci, G., Venturi, G., et al. 2019, A&A, 622, A146, doi: [10.1051/0004-6361/201834372](https://doi.org/10.1051/0004-6361/201834372)
- Mullaney, J. R., Alexander, D. M., Fine, S., et al. 2013, MNRAS, 433, 622, doi: [10.1093/mnras/stt751](https://doi.org/10.1093/mnras/stt751)
- Müller-Sánchez, F., Comerford, J., Stern, D., & Harrison, F. A. 2016, ApJ, 830, 50, doi: [10.3847/0004-637X/830/1/50](https://doi.org/10.3847/0004-637X/830/1/50)
- Müller-Sánchez, F., Prieto, M. A., Hicks, E. K. S., et al. 2011, ApJ, 739, 69, doi: [10.1088/0004-637X/739/2/69](https://doi.org/10.1088/0004-637X/739/2/69)
- Nelson, C. H., & Whittle, M. 1996, ApJ, 465, 96, doi: [10.1086/177405](https://doi.org/10.1086/177405)
- Nevin, R., Comerford, J. M., Müller-Sánchez, F., Barrows, R., & Cooper, M. C. 2018, MNRAS, 473, 2160, doi: [10.1093/mnras/stx2433](https://doi.org/10.1093/mnras/stx2433)
- Oh, S., Colless, M., D'Eugenio, F., et al. 2022, MNRAS, 512, 1765, doi: [10.1093/mnras/stac509](https://doi.org/10.1093/mnras/stac509)
- Oh, S., Colless, M., Barsanti, S., et al. 2024, MNRAS, 531, 4017, doi: [10.1093/mnras/stae1382](https://doi.org/10.1093/mnras/stae1382)
- Polack, G. E., Revalski, M., Crenshaw, D. M., et al. 2024, ApJ, 975, 129, doi: [10.3847/1538-4357/ad71c3](https://doi.org/10.3847/1538-4357/ad71c3)
- Rakshit, S., & Woo, J.-H. 2018, ApJ, 865, 5, doi: [10.3847/1538-4357/aad9f8](https://doi.org/10.3847/1538-4357/aad9f8)
- Riffel, R. A. 2021, MNRAS, 506, 2950, doi: [10.1093/mnras/stab1877](https://doi.org/10.1093/mnras/stab1877)
- Riffel, R. A., Storchi-Bergmann, T., Riffel, R., et al. 2023, MNRAS, 521, 1832, doi: [10.1093/mnras/stad599](https://doi.org/10.1093/mnras/stad599)
- Rodríguez Zaurín, J., Tadhunter, C. N., Rose, M., & Holt, J. 2013, MNRAS, 432, 138, doi: [10.1093/mnras/stt423](https://doi.org/10.1093/mnras/stt423)
- Rupke, D. S. N., & Veilleux, S. 2013, ApJ, 768, 75, doi: [10.1088/0004-637X/768/1/75](https://doi.org/10.1088/0004-637X/768/1/75)
- Ruschel-Dutra, D., Storchi-Bergmann, T., Schnorr-Müller, A., et al. 2021, MNRAS, 507, 74, doi: [10.1093/mnras/stab2058](https://doi.org/10.1093/mnras/stab2058)
- Shin, J., Woo, J.-H., Chung, A., et al. 2019, ApJ, 881, 147, doi: [10.3847/1538-4357/ab2e72](https://doi.org/10.3847/1538-4357/ab2e72)
- Silk, J., & Rees, M. J. 1998, A&A, 331, L1, <https://arxiv.org/abs/astro-ph/9801013>
- Singha, M., Husemann, B., Urrutia, T., et al. 2022, A&A, 659, A123, doi: [10.1051/0004-6361/202040122](https://doi.org/10.1051/0004-6361/202040122)

- Torres-Flores, S., Epinat, B., Amram, P., Plana, H., & Mendes de Oliveira, C. 2011, *MNRAS*, 416, 1936, doi: [10.1111/j.1365-2966.2011.19169.x](https://doi.org/10.1111/j.1365-2966.2011.19169.x)
- Vayner, A., Zakamska, N. L., Riffel, R. A., et al. 2021, *MNRAS*, 504, 4445, doi: [10.1093/mnras/stab1176](https://doi.org/10.1093/mnras/stab1176)
- Veilleux, S., Maiolino, R., Bolatto, A. D., & Aalto, S. 2020, *A&A Rv*, 28, 2, doi: [10.1007/s00159-019-0121-9](https://doi.org/10.1007/s00159-019-0121-9)
- Veilleux, S., Shopbell, P. L., & Miller, S. T. 2001, *AJ*, 121, 198, doi: [10.1086/318046](https://doi.org/10.1086/318046)
- Venturi, G., Marconi, A., Mingozi, M., et al. 2017, *Frontiers in Astronomy and Space Sciences*, 4, 46, doi: [10.3389/fspas.2017.00046](https://doi.org/10.3389/fspas.2017.00046)
- Venturi, G., Nardini, E., Marconi, A., et al. 2018, *A&A*, 619, A74, doi: [10.1051/0004-6361/201833668](https://doi.org/10.1051/0004-6361/201833668)
- Villar-Martín, M., Arribas, S., Emonts, B., et al. 2016, *MNRAS*, 460, 130, doi: [10.1093/mnras/stw901](https://doi.org/10.1093/mnras/stw901)
- Virtanen, P., Gommers, R., Oliphant, T. E., et al. 2020, *Nature Methods*, 17, 261, doi: [10.1038/s41592-019-0686-2](https://doi.org/10.1038/s41592-019-0686-2)
- Vogt, F. P. A., Dopita, M. A., & Kewley, L. J. 2013, *ApJ*, 768, 151, doi: [10.1088/0004-637X/768/2/151](https://doi.org/10.1088/0004-637X/768/2/151)
- Weinberger, R., Springel, V., Hernquist, L., et al. 2017, *MNRAS*, 465, 3291, doi: [10.1093/mnras/stw2944](https://doi.org/10.1093/mnras/stw2944)
- Wellons, S., Faucher-Giguère, C.-A., Hopkins, P. F., et al. 2023, *MNRAS*, 520, 5394, doi: [10.1093/mnras/stad511](https://doi.org/10.1093/mnras/stad511)
- Woo, J.-H., Bae, H.-J., Son, D., & Karouzos, M. 2016, *ApJ*, 817, 108, doi: [10.3847/0004-637X/817/2/108](https://doi.org/10.3847/0004-637X/817/2/108)
- Woo, J.-H., Son, D., & Bae, H.-J. 2017, *ApJ*, 839, 120, doi: [10.3847/1538-4357/aa6894](https://doi.org/10.3847/1538-4357/aa6894)
- Woo, J.-H., Son, D., & Rakshit, S. 2020, *ApJ*, 901, 66, doi: [10.3847/1538-4357/abad97](https://doi.org/10.3847/1538-4357/abad97)
- Wylezalek, D., Flores, A. M., Zakamska, N. L., Greene, J. E., & Riffel, R. A. 2020, *MNRAS*, 492, 4680, doi: [10.1093/mnras/staa062](https://doi.org/10.1093/mnras/staa062)
- Wylezalek, D., Vayner, A., Rupke, D. S. N., et al. 2022, *ApJL*, 940, L7, doi: [10.3847/2041-8213/ac98c3](https://doi.org/10.3847/2041-8213/ac98c3)
- Zubovas, K., & King, A. 2012, *ApJL*, 745, L34, doi: [10.1088/2041-8205/745/2/L34](https://doi.org/10.1088/2041-8205/745/2/L34)